J. Fluid Mech. (2001), *vol.* 441, *pp.* 139–168. Printed in the United Kingdom

The response of a mixing layer formed between parallel streams to a concomitant excitation at two frequencies

By MING DE ZHOU AND I. WYGNANSKI†

Aerospace and Mechanical Engineering Department, University of Arizona, Tucson, AZ 85721, USA

(Received 7 September 1999 and in revised form 14 February 2001)

Simultaneous excitation of a turbulent mixing layer by two frequencies, a fundamental and a subharmonic, was investigated experimentally. Plane perturbations were introduced to the flow at its origin by a small oscillating flap. The results describe two experiments that differ mainly in the amplitudes of the imposed perturbations and both are compared to the data acquired while the mixing layer was forced at a single frequency.

Conventional statistical quantities such as: mean velocity profiles, widths of the flow, turbulent intensities, spectra, phase-locked velocity and vorticity fields, as well as streaklines were computed. The rate of spread of the flow under concomitant excitation at the two frequencies was much greater than under a single frequency, although it remained dominated by two-dimensional eddies. The Reynolds stresses and turbulence production are associated with the deformation and orientation of the large coherent vortices. When the major axis of the coherent vortices starts leaning forward on the high-speed side of the flow, the production of turbulent energy changes sign (i.e. becomes negative) and this results in the flow thinning in the direction of streaming. It also indicates that energy is extracted from the turbulence to the mean motion. Resonance phenomena play an important role in the evolution of the flow. A vorticity budget showed that the change in mean vorticity was mainly caused by the nonlinear interaction between coherent vorticities. Nevertheless, the locally dominant frequency scales the mean growth rate, the inclination and distortion of the mean velocity profiles as well as the phase-locked vorticity contours.

1. Introduction

The turbulent mixing layer serves as a prototypical free shear flow and it has therefore been frequently investigated. At first, the research was limited to a statistical description of the flow, but since the 1960s, it gradually focused on conditional statistics and on coherent structures (Wygnanski & Fiedler 1970; Brown & Roshko 1974; Winant & Browand 1974; Browand & Weidman 1976; Wygnanski *et al.* 1979; Hussain 1983; etc.). After it was realised that the coherent structures play a central role in the evolution of the turbulent mixing layer, artificial excitation was soon to follow (Oster *et al.* 1978; Ho & Huang 1982; Oster & Wygnanski 1982; Fiedler & Mensing 1985; Gaster, Kit & Wygnanski 1985). The experimental procedures adapted were similar to those used in defining the stability of laminar flows (Sato 1960; Browand

† Also at: Faculty of Engineering, Tel Aviv University, Ramat-Aviv, 69978 Israel.

1966; Freymouth 1966; etc.) Fiedler *et al.* (1981), Oster & Wygnanski (1982) and Monkewitz & Huerre (1982) used parallel, linear stability analysis to predict the most amplified frequencies and the amplification rates of the large eddies in the externally excited turbulent mixing layer. Others used modelling and numerical simulation to obtain similar results (Patnaik, Sherman & Corcos 1976; Acton 1976; Ashurst 1979; Riley & Metcalfe 1980; Corcos & Sherman 1984; Inoue & Leonard 1987; Inoue 1989). Gaster *et al.* (1985) have demonstrated the significance of flow-divergence on the evolution of the large, turbulent coherent structures and the ability of the stability approach to predict them in great detail. All of these articles revealed that selective, periodic disturbances strongly influence the coherent structures in the flow and its development in the direction of streaming. Weakly nonlinear analysis that was applied to laminar flow (Kelly 1967; Monkewitz & Huerre 1982) suggested that a turbulent mixing layer might be more sensitive to an external excitation by two frequencies, a fundamental and its subharmonic, because the amplification of the latter could be affected by the presence of the former. Experiments (Zhang, Ho & Monkewitz 1984; Wygnanski & Petersen 1987) and numerical simulations (Inoue 1989, 1992) revealed that a concomitant periodic forcing at these two frequencies affected the evolution of coherent structures and increased the spreading rate of the mean flow beyond the values attained by single-frequency excitation.

The role of the mixing layer in controlling separation was reinforced recently by the quest to delay flow separation through controlled periodic perturbations. The relation was first articulated by Katz, Nishri & Wygnanski (1989) and by Neuburger & Wygnanski (1988) who showed that detached flow forms a mixing layer that separates between a 'dead-water' region adjacent to the surface and a constant velocity stream further away from it. The mean streamlines in the 'free stream' above such a mixing layer are not curved and they do not diverge in the direction of streaming. Consequently, we would like to generate a sufficient pressure difference across this mixing layer forcing it to bend toward the surface. This may be attained by enhancing the entrainment (pumping) of fluid by the mixing layer from the limiting reservoir of fluid bound by it and by the solid surface. Thereafter, the continuous pumping action of the large eddies scouring the surface may keep the mixing layer adjacent to the surface. We are interested, therefore, in exploring the role of the dual frequency excitation in promoting flow reattachment and in its maintenance.

Since the mixing layer is, perhaps, the simplest turbulent shear flow occurring in nature, a better understanding of its features may improve our understanding of turbulence in general. For example, what is the role of large coherent structures in the production of turbulence, how does it relate to nonlinear wave interactions, how do we assess the interrelation between coherent structures and typical random quantities? The measurements carried out by I. Weisbrot (unpublished Tel Aviv University 1984) provide some information on the above-mentioned problems. For example, the various Reynolds stresses (both coherent and incoherent) have been carefully scrutinized in order to explain the dependence of the flow on coherent structures and on the various interactions among them.

2. Experimental considerations

The experiments were carried out in a facility described by Oster & Wygnanski (1982) and slightly modified by Weisbrot & Wygnanski (1988), where the effects of single-frequency excitation were investigated extensively and the meaning of 'pairing' under dual-frequency excitation was discussed. Three sets of data are acquired. They

represent a mixing layer formed between two parallel streams of different velocities whose ratio, $R = (U_1 - U_2)/(U_1 + U_2) = 0.25$ throughout. Measurements were made across the flow starting at $x = 200$ mm from the splitter plate and terminating at $x = 1720$ mm, thus encompassing three-quarters of the 2 m long test section in order to avoid undesirable end effects, particularly near the exit. The streamwise interval between adjacent measuring stations was only 20 mm in order to resolve spatially the large coherent structures in the flow. The boundary layers on both sides of the splitter plate were turbulent. The flow was excited by a small flap hinged to the trailing edge of the splitter plate and oscillating at a maximum amplitude of 4 mm. This provided a maximum initial (measured $x = 200$ mm) mean coherent disturbance level summed over both directions of approximately 7%. To obtain this number, the phase-locked ensemble-averaged and filtered streamwise and normal velocity perturbations were integrated across the flow and divided by the width of the measuring region of the mixing layer and its average velocity, i.e.

$$A_f = \frac{\int_{y_{\min}}^{y_{\max}} \sqrt{\langle u \rangle^2 + \langle v \rangle^2}\,\mathrm{d}y}{\frac{1}{2}(y_{\max} - y_{\min})(U_2 + U_2)}$$

Two components of velocity were measured instantaneously at 7 transverse locations across the mixing layer by using a hot-wire rake containing 14 wires configured in 7 $\times$-wire arrays. The rake was traversed across the flow until the velocity gradients and the turbulent intensities vanished. Two reference signals and all individual velocity components were digitized and stored. The lowest-frequency forcing signal was used as a reference to ensemble-average the data.

In order to check the experimental procedure (i.e. repeat earlier experiments) and provide data at sufficiently small spatial resolution, the excitation for the first data set was made at a single (fundamental) frequency and is hereinafter referred to as the SF case. The free-stream velocities selected were 10 and 6 m s^{-1}, respectively, as in previous experiments. The excitation frequency of 45 Hz was chosen as it provided a perturbation that had undergone its maximum amplification (i.e. it became neutrally stable) in the centre of the test section. The displacement amplitude of the fliperon, that provided an average 4.8% excitation-level at the first measuring station, was only 1.5 mm. When the real experiment started at two concomitant frequencies of excitation, this level of initial, threshold disturbance demanded too high a displacement amplitude from the flap thus contaminating the initial signal with other harmonics. It was therefore decided to lower the velocities to 8 and 4.8 m s^{-1}, respectively while maintaining the same velocity ratio $R = 0.25$. The excitation frequency had to be reduced to $f = 36$ Hz in order to change the wavelength of the disturbance, ($\lambda = (U_1 + U_2)/2f$), and thus maintain the dimensionless scaling parameter for the single-frequency excitation, Rx/λ, unchanged.

When the oscillating flap was excited simultaneously by the two frequencies at its maximum 'clean' displacement amplitude of 4 mm at the lower tunnel speed, the combined amplitude level of the phase-locked disturbance was 7.1%. In that case, the displacement-amplitude of the fliperon at both frequencies was almost identical. The disturbance level of the two frequencies at the initial measuring station (200 mm downstream of the fliperon's trailing edge and corresponding approximately to a single wavelength of the fundamental perturbation) was also close (5.2% versus 4.9%). This data set was labelled 'two frequencies-strong' (TFS). In view of the unexpected characteristics of this mixing layer, it was decided to reduce the total

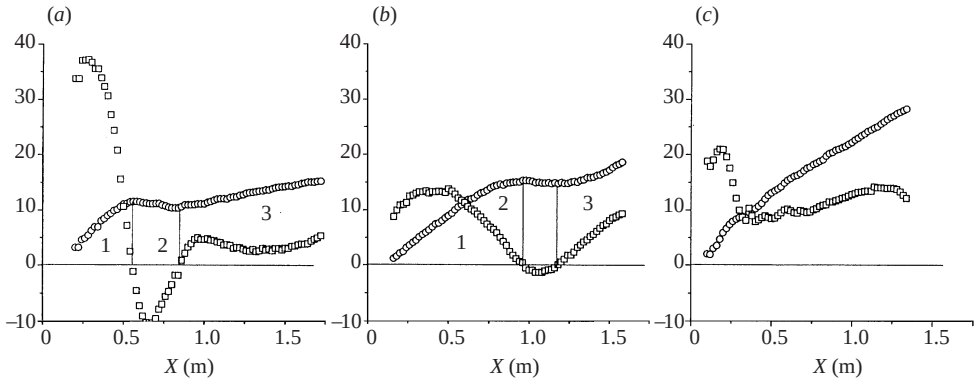

FIGURE 1. Momentum thickness and integration of production across the layer. (*a*) SF. (*b*) TFW. (*c*) TFS. ○, momentum thickness θ (mm); □, $\int \overline{u'v'}(\partial U/\partial y)\mathrm{d}y/50$ ($\mathrm{m^3\,s^{-3}}$).

level, of excitation to half of its original, 3.4%. This case is referred to as 'two frequencies-weak' (TFW).

The phase between the two perturbations was maintained constant at both excitation levels, because it was believed that the divergence of the mean flow would preclude the possibility of resonance. This opinion was formed because the phase velocity of any unstable disturbance in a divergent mean flow varies with x and y (Crighton & Gaster 1976; Gaster *et al.* 1985). However, this view was altered later, when Paschereit, Wygnanski & Fiedler (1995) demonstrated experimentally that partial resonance (i.e. not across the entire flow) is possible in an axisymmetric, divergent mixing layer and that it depends on the initial phase angle between the fundamental and the subharmonic frequency.

The instantaneous velocity was decomposed into a time mean quantity, a phase locked fluctuation $\langle u \rangle$ and the random residue: $u = U + \langle u \rangle + u_r$. We are fully aware that the coherent portion of the motion may be smeared-out by phase jitter and therefore poorly represented by a phase-locked and ensemble-averaged quantity (Zhou, Heine & Wygnanski 1996). However, the phase jitter of the dominant structures in the present flows was quite small. The coherent energy and Reynolds stresses obtained from simple, phase-locked data and from the more complex, temporal pattern matching (Zhou *et al.* 1996), were not materially different. Consequently, only the conventional phase-locked and ensemble-averaged results are presented. Various aspects of the coherent motions, including phase-locked turbulent energy and Reynolds stress, phase and amplitude distributions of the individual components of the disturbances, coherent vorticity contours and coherent streaklines were calculated from the data. Based on these results, the relation between coherent motions and the growth of the layer was observed.

3. Results and discussion

3.1. *The mean flow*

Streamwise distributions of the momentum thickness (this is an integral lengthscale whose integrand vanishes at both integration limits).

$$\theta = \int_{-\infty}^{\infty} \frac{U - U_1}{U_2 - U_1}\left[1 - \frac{U - U_1}{U_2 - U_1}\right] \mathrm{d}y,$$

are shown in figure 1 for the three different excitations considered. Although the

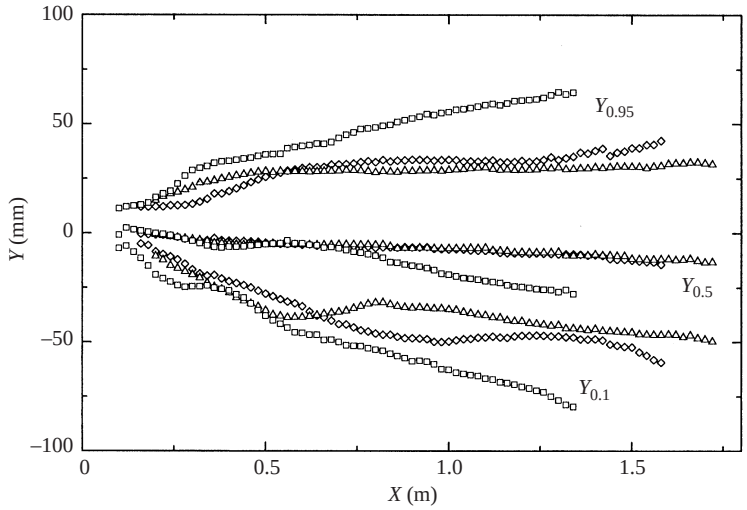

FIGURE 2. Streamwise distribution of the boundary. △, SF; ◇, TFW; □, TFS.

abscissa, x, in this and other figures is dimensional it may be converted to a dimensionless R_x/λ_f by multiplying the distance in metres by 1.406. It can be seen that the rate of spread of these flows differs from case to case, and also from region to region in a single case. When the mixing layer was excited by a single frequency (labelled SF) the momentum thickness increased up to $x = 560$ mm from the trailing edge of the splitter plate (region 1 according to Oster & Wygnanski 1982). It then ebbed and decreased with increasing streamwise direction up to $x = 840$ mm (region 2). Thereafter, it resumed its growth but at a lower rate. The data set labelled 'two frequencies-weak' (TFW) shows a similar trend; however, its growth rate in region 1 is slightly smaller than the SF set. Its rate of spread in region 3, however, is almost identical to that in region 1 and considerably larger than the corresponding region for the SF excitation. Furthermore, the onset of region 2 starts further downstream in this flow ($x = 950$ mm), nevertheless the final width of the flow at $x = 1580$ mm was 25% larger than in the SF set. The momentum thickness resulting from stronger excitation (the 'two frequencies-strong' (TFS) case) increases monotonically in the direction of streaming, nevertheless, the initial rate of growth for $x < 300$ mm is much larger than the final one. The final rate of growth in this case is almost the same as the final rate of growth in the TFW experiment. It is clear that strong, concomitant excitation at two frequencies can double the final width of the flow relative to the single-frequency excitation.

The different rates of spread plotted in figure 1 show the dependence of the mean flow on the excitation conditions. The spreading rate is tied, in turn, to the turbulence production and, therefore, the latter is also plotted in figure 1 and will be discussed later. In order to pinpoint the regions most affected by the external excitation, the borders and the centre of the mixing layer were arbitrarily defined by three numbers expressing the location on the mean velocity profile: $Y_{0.1}$, $Y_{0.95}$ and $Y_{0.5}$ representing the y-locations where the local mean velocity $(U - U_1)/(U_2 - U_1) = 0.1$, 0.95 and 0.5. They represent both borders of the mixing layer and its centre, they are plotted in figure 2. The lateral rate of spread of $Y_{0.95}$ was initially (for $x < 330$ mm) quite rapid for the SF excitation and for the TFS case, but it was almost nil for the TFW excitation. At $330 < x < 550$ mm the lateral rate of spread of $Y_{0.95}$ increased for the

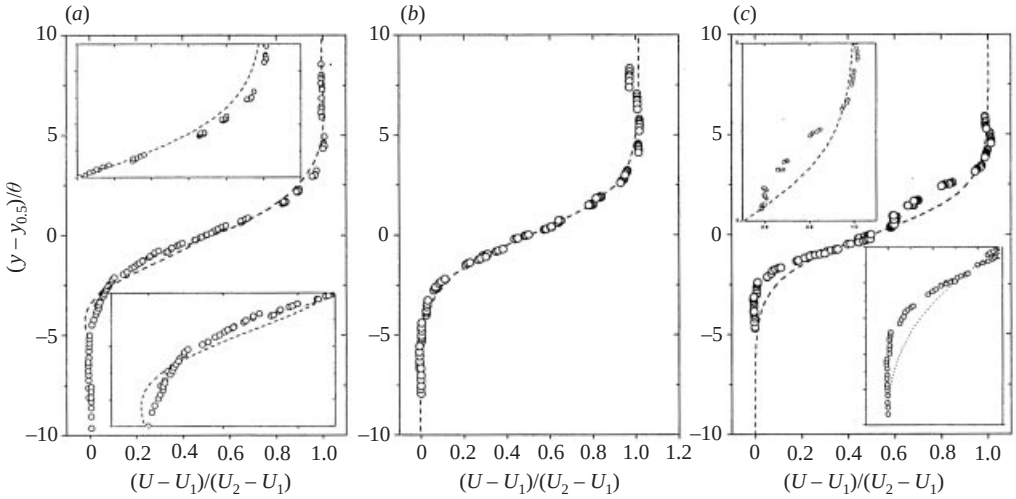

FIGURE 3. Comparison between upstream and downstream regions of the normalized mean velocity profiles. (*a*) SF. – – –, 0.2 m $< x <$ 0.56 m; ○, 0.84 m $< x <$ 1.72 m. (*b*) TFW. – – –, 0.16 m $< x <$ 0.9 m; ○, 1.24 m $< x <$ 1.58 m. (*c*) TFS. – – –, 0.1 m $< x <$ 0.24 m; ○, 1.06 m $< x <$ 1.34 m.

TFW excitation while it decreased for the other two cases. For $550 < x < 1340$ mm, $Y_{0.95}$ stopped its lateral rate of spread in the TFW and SF excited flows, but it increased its rate of spread for the TFS flow.

Whereas $Y_{0.5}$ was identical for the TFW and SF excited flows through the entire range of streamwise distances considered, it was displaced laterally toward the low-speed stream for the TFS excitation at $x > 550$ mm. The lateral divergence between $Y_{0.95}$ and $Y_{0.5}$ that occurred at $x > 550$ mm for the TFS test was largely responsible for the final width of this flow at the end of the measurement domain. In contrast, the SF excitation resulted in the convergence between $Y_{0.1}$ and $Y_{0.5}$ at $550 < x < 840$ mm that reduced the width of the flow in this range (region 2 in figure 1). $Y_{0.1}$ maintained its lateral rate of spread for the TFW flow up to $x = 950$ mm and was responsible for the increased width of the mixing layer relative to the SF excitation. $Y_{0.1}$ resumed its lateral growth for this case only beyond $x > 1400$ mm, while in the interim ($950 < x < 1400$ mm) it remained constant or even decreased slightly (figure 2). Consequently, whereas for TFW and SF excitation most of the spreading rate (and presumably mixing) occurs on the low-velocity side of the flow, it switches sides in the TFS case. This observation deserves special attention as it may lead to improved mixing through the use of active flow control. We may also note that $Y_{0.1}$ undulates for the TFS case up to $X \approx 600$ mm, beyond which it spreads laterally in a linear fashion as it does in an unexcited mixing layer.

Normalized mean velocity profiles, $(U - U_1)/(U_2 - U_1)$, corresponding to the three types of excitation are shown in figure 3. The ordinate in figure 3 is $(Y - Y_{0.5})/\theta$, and it is consistent with the definition of the centre of the mixing layer. The velocity profiles in each region are self-similar, but the similarity does not extend throughout the domain of measurement (i.e. between regions). For SF forcing, the slope of the velocity profile, $\mathrm{d}U/\mathrm{d}Y$ on the low-speed side of region 1 (dashed line) is larger than in region 3 (see symbols in figure 3*a*) while the opposite effect is seen on the high-speed side. For TFW forcing, there is almost a perfect self-similarity between regions 1 and 3 (figure 3*b*). In the case of TFS forcing at $X > 1000$ mm region (it is

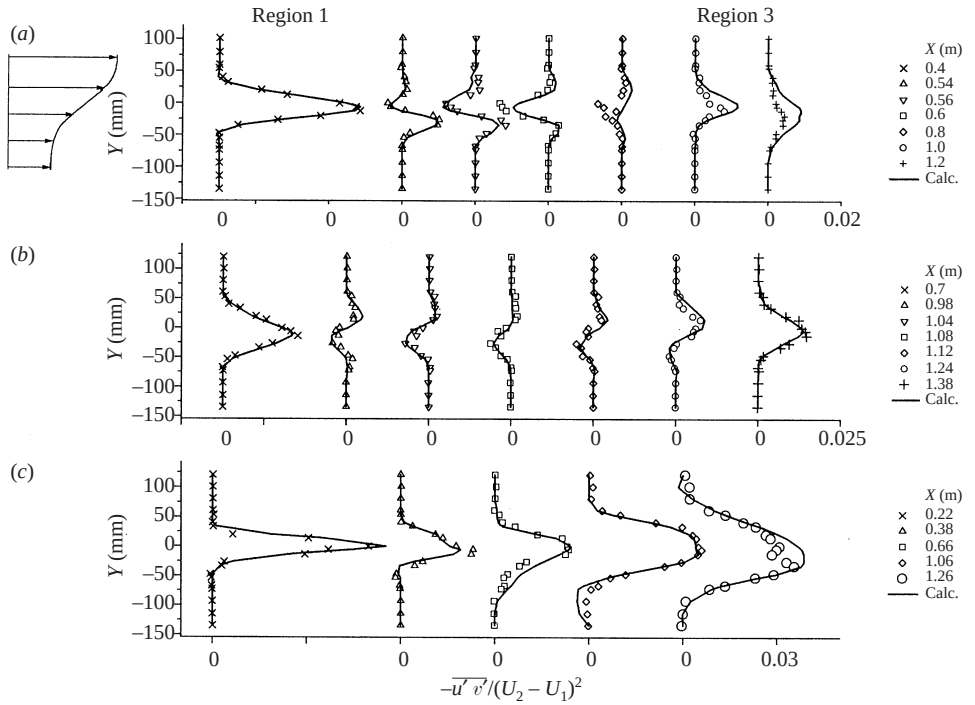

FIGURE 4. Reynolds stress distribution. (*a*) SF. (*b*) TFW. (*c*) TFS.

impossible to discuss this flow in terms of three distinct regions), there is a strong kink in the mean velocity profile on the high-speed side that moves toward the centre with increasing x (figure 3*c*). This deformation is closely related to the type of coherent motion dominating the flow in a given region, as will be discussed later.

3.2. *Reynolds stress and turbulent intensities*

The lateral distributions of Reynolds stress and two components of the turbulent intensity are shown in figures 4–6 for the three flows considered. The first and last streamwise locations chosen correspond to regions 1 and 3 while the intermediate locations represent data taken in region 2 and its boundaries (i.e. transition regions between 1 and 2 and 2 and 3).

The Reynolds stresses are positive in regions 1 and 3 for SF and TFW (figure 4*a*, *b*) where the momentum thickness also increases (see figure 1). However, the sign of the Reynolds stress changes in region 2 and it is associated with a decrease of the momentum thickness in the direction of streaming. Typically, close to the end of region 1 of the SF case (i.e. for $X \cong 540$ mm in Fig. 2.1a), the shear stress on the high-speed side of the mixing layer becomes gradually negative. At $X = 560$ mm, $\mathrm{d}\theta/\mathrm{d}X = 0$ and the integral of the shear stress across the layer vanishes as well. Around $X = 800$ mm the Reynolds stress becomes positive again and with it $\mathrm{d}\theta/\mathrm{d}X > 0$. This location marks the transition to region 3 in figure 1. We may observe that the maximum negative value of $u'v'$ occurs in the centre of the mixing layer in the SF case (figure 4*a*).

The results for the TFW excitation are similar to the SF flow, in particular, the correlation between the integral of the Reynolds stress across the flow and the location corresponding to $\mathrm{d}\theta/\mathrm{d}X = 0$. In region 2 (e.g. at $X = 1080$ mm), the shear stresses are

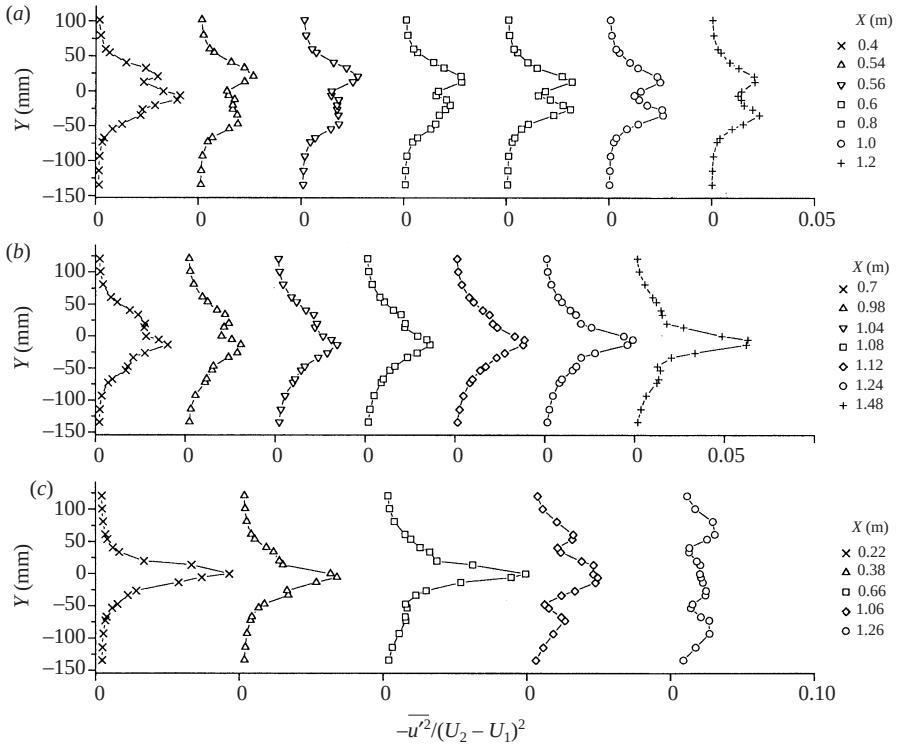

FIGURE 5. Turbulence energy distribution, u-component. (a) SF. (b) TFW. (c) TFS.

negative across the layer. At $X > 1120$ mm, transition from regions 2 to 3 occurs and the Reynolds stress becomes positive again (figure 4b). There are, however, interesting differences between the TFW and the SF cases during the transition from regions 1 to 2. In the TFW flow, the negative shear stress appears first on the low-speed side and remains there throughout region 2 and the transition region between 2 and 3. For the SF flow the negative shear stress appears first in the centre, above (on the high-speed side) the region of positive Reynolds stress. The transition from regions 2 to 3 is associated with the generation of a new zone of positive Reynolds stress on the high-velocity side of the flow. This region diffuses toward the low-speed side of the mixing layer with increasing X. Thus, whenever the Reynolds stress distribution has an S shape in the TFW case, the zone of positive stress is always on the high-speed side (see the lateral stress distributions at $X = 1040$ and 1120 mm in figure 4b) while it switches from side to side in the SF experiment. In the TFS experiment $\mathrm{d}\theta/\mathrm{d}X > 0$ everywhere, and thus the integral of the shear stress never changes its sign. Out of the five locations plotted in figure 4(c), the first two are in a region of locally decaying Reynolds stress, while the last three are in a region of local amplification. It will be seen later that the abrupt increase in Reynolds stress for the last three locations is related to a corresponding change in the form of the coherent structures.

The corresponding distributions of the u' and v' are plotted in figures 5 and 6. For the SF excitation the distribution of the u' at a given X contains two maxima separated by a saddle point in the centre (see figure 5a at $X = 540$ and $X > 600$ mm) while the v' distribution contains a single maximum at the centre of the flow (figure 6a). Such intensity distributions are indicative of a single row of travelling vortices. A

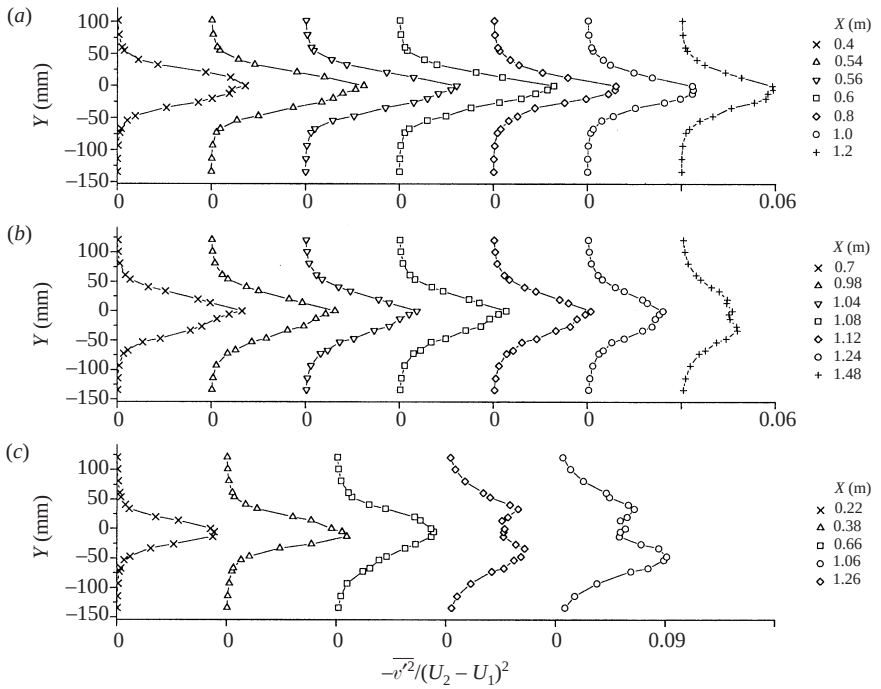

FIGURE 6. Turbulence energy distribution, v-component. (*a*) SF. (*b*) TFW. (*c*) TFS.

similar observation can be made for the TFW excitation around $X \approx 980$ mm. On the other hand, for the TFW flow at $X > 1400$ and for the TFS flow at $X \approx 660$, the u' distribution develops peaks while the v' distribution becomes broad and eventually develops two maxima with a saddle point in between. Further downstream the u' distribution develops three maxima while the v' distributions have two (figures 5*c* and 6*c*). These distributions suggest that a vortex pairing take place in which some of the vortices that were originally in line became displaced laterally. When the initial displacement is comparable to a typical vortex radius, the u' component develops a strong peak in the centre, but as the displacement increases this peak may split into three (figure 5*c*, $X = 1060$ mm).

The integrated values of u'^2, v'^2 and $u'v'$ across the layer are shown in figure 7. Most interesting is the correlation between the sign of the integrated Reynolds stress and $\mathrm{d}\theta/\mathrm{d}X$ (figure 1). Whenever $\int u'v'\mathrm{d}Y < 0$ so is $\mathrm{d}\theta/\mathrm{d}X$. The local maxima and minima of θ match the zero crossings of $\int u'v'\mathrm{d}Y$ perfectly for the SF and TFW experiments. In a mixing layer, θ represents an integral lengthscale whose integrand vanishes on both sides of the flow, thus the relationship between $u'v'$ and θ differs from the relationship we are accustomed to in a boundary layer. However, since $\mathrm{d}U/\mathrm{d}Y$ in a mixing layer is always positive, the sign of shear stress determines the sign of the turbulence production. For this reason, the integrated turbulence production term $\int u'v'(\mathrm{d}U/\mathrm{d}Y)\mathrm{d}Y$ is plotted in figure 1.

The integral value of $\int(u')^2\mathrm{d}Y$ is hardly amplified for the SF excitation before starting to decay slowly with increasing X. In the TFW case, the value of $\int(u')^2\mathrm{d}Y$ increased by 50%, reached a plateau, and then increased again when $\int(u'v')\mathrm{d}Y > 0$. The value of $\int(v')^2\mathrm{d}Y$ in this case, attained an amplification of 440% just prior to the location at which $\int(u'v')\mathrm{d}Y$ became negative at $X = 950$. In the TFS case the

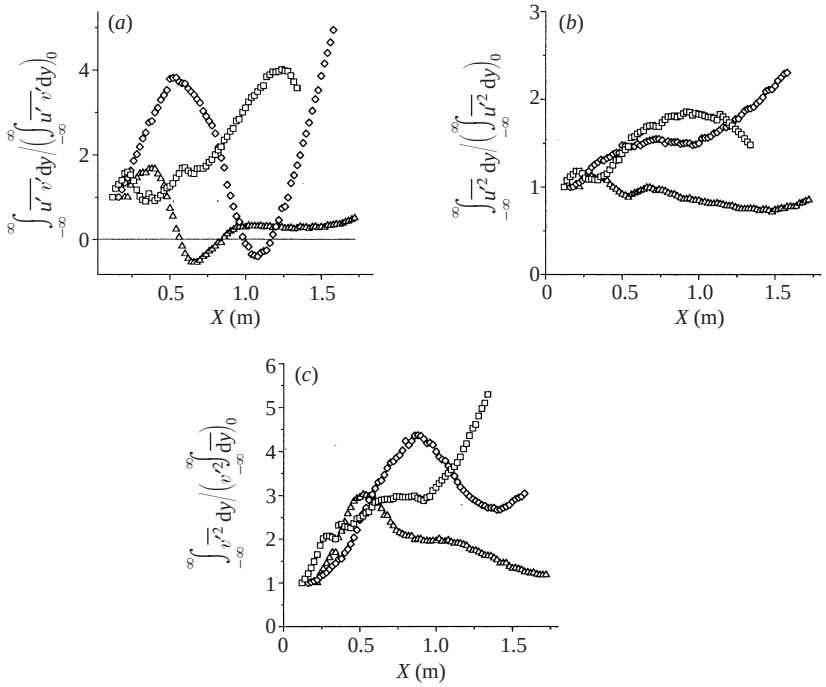

FIGURE 7. Integration of turbulence quantities across the layer. △, SF; ◇, TFW; □, TFS.

amplitude of $\int (v')^2 \mathrm{d}Y$ increased in a stepwise manner, first by a factor of 2, then to 3 before resuming continuous growth and attaining a factor of 5.5 at the end of the measurement domain.

There is an exchange of energy between the two components of turbulence intensity that is most obvious for the SF excitation. For example: a saddle point in the $\int (u')^2 \mathrm{d}Y$ occurring at $X = 550\,\mathrm{mm}$, corresponds to a maximum in the $\int (v')^2 \mathrm{d}Y$. The relationship between the two fluctuating components in the TFW and TFS experiments is subtler but it exists nontheless. These relationships imply that significant energy is contained in large two-dimensional eddies as already observed by Gaster *et al.* (1985). These relationships will be better understood when the phase-locked and ensemble-averaged data of a given scale is processed.

3.3. *Mean momentum balance*

In order to check the two-dimensionality of the flow and to some extent the reliability of the measurements, the Reynolds stress distributions were calculated from the two-dimensional momentum equation:

$$-\frac{\overline{uv}}{(U_2 - U_1)^2} = \frac{1}{(U_2 - U_1)^2} \int_{-\infty}^{y} \left[\bar{U} \frac{\partial \bar{U}}{\partial x} + \bar{V} \frac{\partial \bar{U}}{\partial y} + \frac{\partial}{\partial x}(u'^2 - v'^2) \right] \mathrm{d}y,$$

while the continuity equation yields:

$$\bar{V} = -\int_{-\infty}^{y} \frac{\partial \bar{U}}{\partial x} \mathrm{d}y + V_{-\infty}$$

where,

$$\frac{V_{-\infty}}{U_2 - U_1} = \frac{1}{(U_2 - U_1)^2} \int_{-\infty}^{\infty} \frac{\mathrm{d}}{\mathrm{d}x} [(\bar{U} - U_1)\bar{U} + u'^2 - v'^2] \mathrm{d}y.$$

The integration was initiated on the high-speed side from an Y location corresponding to a vanishing velocity gradient. The normal mean velocity component V, used in the momentum balance was not measured but rather calculated from the continuity equation because measurements of V with hot wires are notoriously inaccurate in turbulent shear flows. The values of V at infinity were determined by an iterative procedure requiring that the Reynolds stress on the opposite side of integration domain will vanish. This criterion was independent of the side at which the integration was initiated. The entrainment field results in a pressure gradient that is neglected by the boundary-layer approximation. Dropping the pressure gradient at the integration boundaries resulted in an error that was most apparent at the boundaries. Thus, a free-stream pressure gradient was imposed at the boundaries of the integration. Since the streamwise velocity gradients on the high-speed boundary of the flow are not the same as on the low-speed side, the local pressure gradient was calculated from linearly interpolated values across the layer.

The results of these calculations are marked by solid curves in figure 4. There is good agreement between calculations and measurements for the TFW and TFS cases throughout the measurement domain and in region 1 of the SF experiment where the calculated positive Reynolds stress matches the measured data very well. In the transition regions marking the boundaries between 1 and 2 or 2 and 3 of SF, the calculated shear stresses match all the important features of the experiment, including the appearance of the negative shear stress starting on the high-speed side of the flow. At $x = 560\,\text{mm}$, where $\mathrm{d}\theta/\mathrm{d}X = 0$, the integral of the calculated shear stress across the layer also vanished. In region 3, however, there is a considerable discrepancy between the calculated Reynolds stress and the data measured for the SF experiment. This raises some questions about the two-dimensionality of the flow near the end of the measurement domain where the coherent eddies become weak.

3.4. *Spectra*

The existence of coherent structures in turbulent flows can be detected through spectral analysis. Even in the absence of external excitation, a spectral peak appearing in the low-frequency range can often be identified with a wavy disturbance that had undergone the largest possible amplification. These predominant frequencies may vary somewhat across the flow because of its divergence in the direction of streaming (Crighton & Gaster 1976). Spectral analysis can provide extensive information about energy transfers that take place in externally excited flows.

The power spectra of the v' fluctuations and the cross-spectra of $u'v'$ measured at various x-locations close to the centreline of the layer are shown in figures 8 and 9. The power spectra of u' are not shown for the sake of brevity because, for a two-dimensional perturbation, the two distributions (u' and v') are related through continuity and are usually delayed in phase.

For the SF excitation, the fundamental frequency dominates the entire flow (figure 8*a*) with a weak harmonic being present at the end of region 1 owing to the relatively large amplitude of the fundamental. No subharmonic frequency was observed suggesting that 'vortex pairing' is inhibited by the single-frequency harmonic excitation. The cross-spectrum is also dominated by the excitation frequency even though it is an order of magnitude weaker than the power spectrum (figure 9*a*). The streamwise location at which the cross-spectrum becomes negative (indicating the possible existence of a negative Reynolds stress) corresponds to the location at which v' attained its maximum amplitude. Consequently, this is the location at which the mean flow became neutrally stable relative to the imposed disturbance.

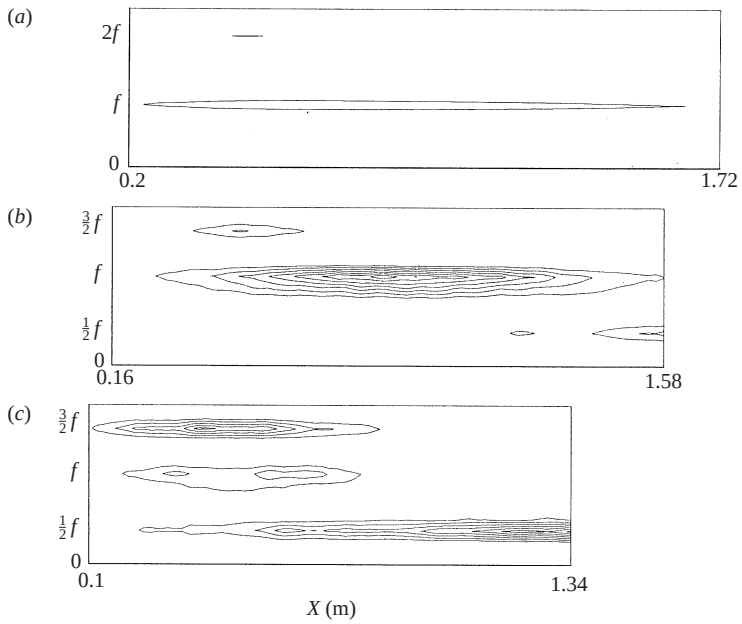

FIGURE 8. Power spectra of the turbulence energy (v-component). Amplitude level, 0–15 m^2s^{-2}. (*a*) SF. (*b*) TFW. (*c*) TFS.

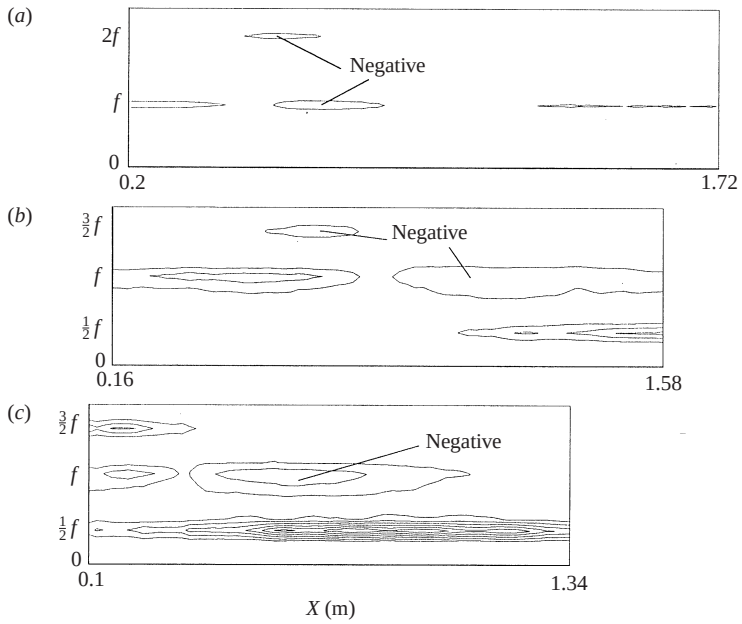

FIGURE 9. Spectra of Reynolds shear stress. Amplitude level, −0.7–3.5 m^2s^{-2}. (*a*) SF. (*b*) TFW. (*c*) TFS.

Similar observations can be made for the TFW case, except that the peak in the power spectrum at the fundamental frequency is much higher and it occurs at a larger streamwise location (figure 8*b*). Two additional observations can be made:

(i) The streamwise amplification of the subharmonic disturbance might not have

attained its maximum at the end of the measurement domain because it was not initially amplified. Note that the subharmonic excitation is hardly distinguishable from the background over 60% of the measurement domain (figures 8*a* and 9*a*). We can correlate this with the low initial amplification rate of the integrated intensity $\int v'^2 \mathrm{d}y$ (figure 7) observed at small distances for the TFW case.

(ii) On the other hand, there is an early appearance of a wavy disturbance generated by the interaction of the two excited modes (i.e. $\frac{3}{2}$ of the fundamental frequency). This suggests a transfer of energy from the imposed excitation to the interaction mode. Once again, the location of the peak in the power spectrum corresponds to the onset of a negative cross-spectrum at f and $\frac{3}{2}f$.

In the TFS case there is an early dominance of the $\frac{3}{2}f$ perturbation that overshadows the fundamental in spite of the fact that the latter frequency was externally forced upon the flow (figure 8*c*). The disturbance at the fundamental frequency, f, attained its first maximum level around $X = 340\,\mathrm{mm}$, while the peak at the interaction frequency occurred soon thereafter ($X = 400\,\mathrm{mm}$) to be followed by the subharmonic disturbance (around $X = 600\,\mathrm{mm}$). The locations of these peaks in the spectrum correspond also to the locations at which undulations in $\int v'^2 \mathrm{d}y$ occur. A second peak in the fundamental disturbance occurs further downstream (around $X = 650\,\mathrm{mm}$) where the cross-spectrum at that particular frequency is negative. This suggests a strongly nonlinear interaction among these three modes. The negative cross-spectrum at the fundamental frequency corresponds to a local plateau in $\int u'v' \mathrm{d}y$ shown in figure 7. The dominance of the subarmonic ($\frac{1}{2}f$) and the interaction ($\frac{3}{2}f$) modes in the power and cross-spectra for the TFS excitation is another indication that a nonlinear mechanism is responsible for the energy exchanges that take place in this flow. In particular, downstream of the peak in the $\frac{3}{2}f$ power spectrum, there is no corresponding negative cross-spectrum region. It implies that the decay of the $\frac{3}{2}f$ frequency is not due to the negative production or direct energy transfer back to the mean, but rather, due to transfer to other components through nonlinear interactions.

3.5. *Phase-locked and ensemble-averaged data*

We may assume that the coherent structures are represented by phase-locked and ensemble-averaged velocity fluctuations. We may further decompose these coherent fluctuations in Fourier space to obtain the amplitudes of the leading spectral components in the flow. They correspond, of course, to the two forcing frequencies and their sum, since these were also the leading spectral components observed in figure 8.

The spatial distribution of the prevailing disturbances (i.e. the fundamental, f_0, the subharmonic, $\frac{1}{2}f_0$, ,and the leading interaction, $\frac{3}{2}f_0$) are shown in figures 10–12 at some selected streamwise locations. The data corresponding to the SF excitation for $200 < X < 560\,\mathrm{mm}$ such as the amplitude distribution of $\langle u \rangle_{f_0}$ are well known (Gaster *et al.* 1985; Weisbrot & Wygnanski 1988) because they represent a linearly amplifying mode. Around $X \approx 550\,\mathrm{mm}$, this mode ends its amplification cycle and starts to decay. The amplitude and phase distributions, therefore, represent a typical array of eddies that span the entire width of the flow.

The initial evolution (for $X < 700\,\mathrm{mm}$) of the fundamental frequency in the TFW experiment is similar to SF forcing. However, toward the end of the measurement domain (i.e. for $X > 1300\,\mathrm{mm}$.) the amplitude distributions of $\langle u \rangle_{f_0}$ and $\langle v \rangle_{f_0}$ indicate that the array of decaying vortices is being displaced laterally in an orderly-staggered fashion. This is coupled with a typical, distribution of $\langle u \rangle_{f_0/2}$ that is being amplified at $X > 1040\,\mathrm{mm}$. The distributions of f_0 and $\frac{1}{2}f_0$ amplitudes for the TFS excitation are similar to TFW except that they occur much closer to the origin of the flow.

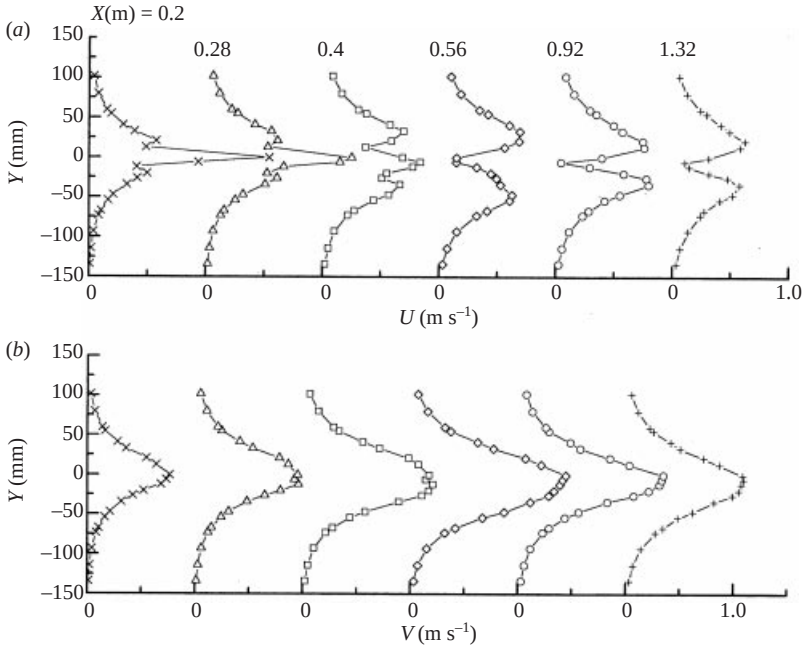

FIGURE 10. Amplitude distribution of the fundamental disturbance (SF).

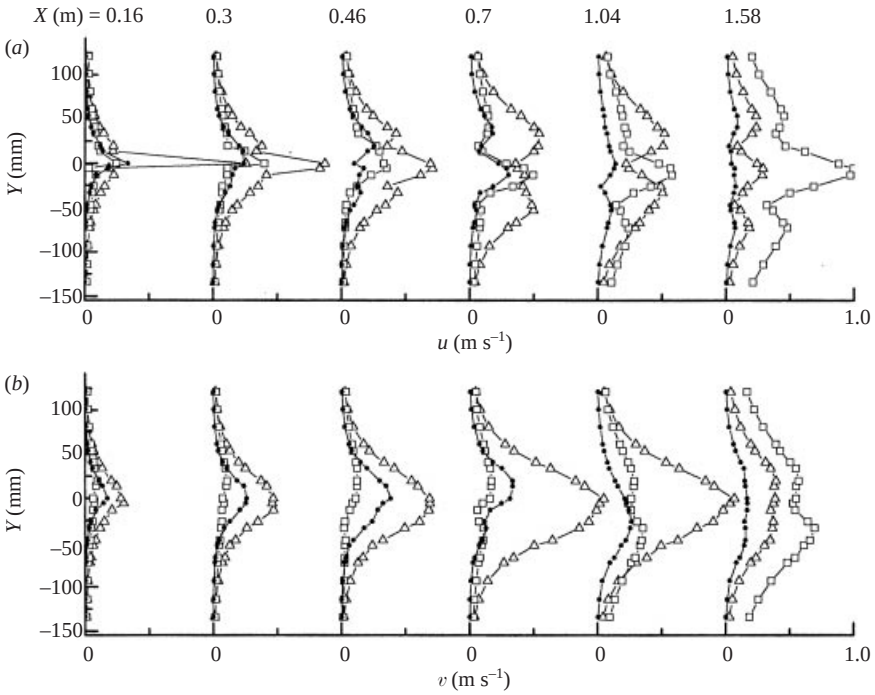

FIGURE 11. Amplitude distribution of the leading frequencies (TFW). △, f_0; □, $\frac{1}{2}f_0$; ●, $\frac{3}{2}f_0$.

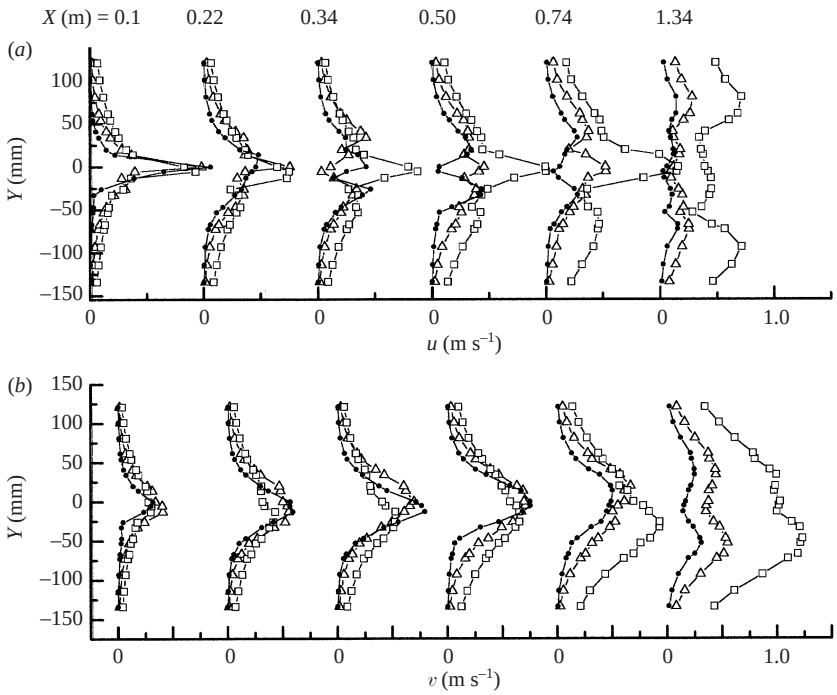

FIGURE 12. Amplitude distribution of the leading frequencies (TFS). △, f_0; □, $\frac{1}{2}f_0$; ●, $\frac{3}{2}f_0$.

The stagger of the decaying vortices associated with the fundamental frequency occurs around $X \approx 400$ mm and it evolves into two separate rows of vortices toward the end of the measurement domain (see the $\langle v \rangle_{f_0}$ distribution in figure 12*b* at $X = 1340$ mm). The amplitude distributions of $\langle u \rangle_{f_0/2}$ or $\langle v \rangle_{f_0/2}$ measured at $X > 1000$ mm in the TFS case are not familiar from linear stability analysis. Note that a very small amplitude of $\langle v \rangle_{f_0/2}$ in the TFW case generates a substantial amplitude of the nonlinear interaction mode $\langle v \rangle_{3f_0/2}$. This is particularly visible in the initial region ($X < 500$ mm in figure 11*b*) where the fundamental frequency is being linearly amplified by extracting energy from the mean motion. At larger distances, most of the energy is being absorbed by the subharmonic $\langle v \rangle_{f_0/2}$. In the TFS case, where the initial amplitude of $\langle v \rangle_{f_0/2}$ is equal to $\langle v \rangle_{f_0}$, the interaction mode $\langle v \rangle_{3f_0/2}$ is of comparable amplitude (see figure 12 for $X < 500$ mm). The relative intensity of the interaction mode, $\langle v \rangle_{3f_0/2}$, in both flows decreased after the subharmonic became the dominant mode (see figures 11 and 12 for $X > 1300$ mm).

The various phase-locked quantities were integrated across the layer to obtain the streamwise variations of the coherent energy contained in the individual modes. The results for $\int \langle u^2 \rangle \mathrm{d}y$, $\int \langle v^2 \rangle \mathrm{d}y$, $\int \langle uv \rangle \mathrm{d}y$ and their leading coherent quantities are shown in figures 13(*a*) to 13(*c*), respectively. The corresponding total turbulent intensities discussed previously are replotted here for comparison. The intial value of $\int \langle u^2 \rangle \mathrm{d}y$ for the SF excitation is approximately 70% of $\int u'^2 \mathrm{d}y$, but it diminishes slowly to 25% at the end of the measurement domain. For the TFW case, the initial level was only 55% yet it increased to 75% at large X, while for the TFS excitation, this ratio remained at approximately constant level of 85% (see figure 13*a*). The ratio between $\int \langle v^2 \rangle \mathrm{d}y$ and $\int (v')^2 \mathrm{d}y$ is usually larger than for the streamwise component of velocity and it exceeds 90% for the TFS excitation. The amplification ratios of the

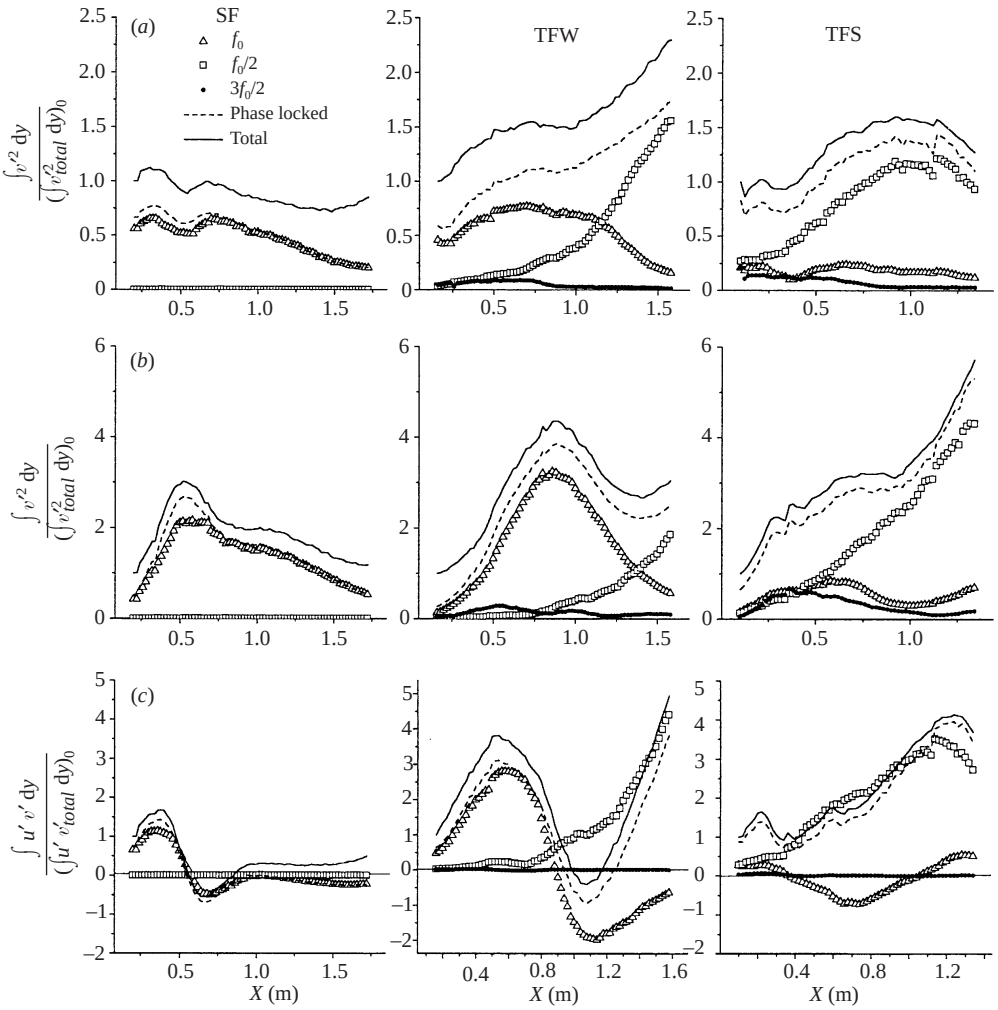

FIGURE 13. Streamwise development of coherent quantities. △, f_0; □, $\frac{1}{2}f_0$; ●, $\frac{3}{2}f_0$; – – –, phase locked; ——, total.

$\langle v\rangle_f$ component at the fundamental frequency are much larger than the amplification of the $\langle u\rangle_f$ component. For the SF case, for example, $\int\langle u^2\rangle_f \mathrm{d}y$ increased over its initial value by a mere 25% in region 1, it increased by 70% in region 1 of the TFW excitation but did not increase at all for TFS (figure 13*a*). The integrated normal component, $\int\langle v^2\rangle_f \mathrm{d}y$, increased by 5-fold for SF, by 20-fold for TFW and only by a factor of 4 for TFS. The disparity in the amplification between the streamwise and normal components made the total, integrated turbulent energy behave like $\int\langle v^2\rangle_f \mathrm{d}y$, thus the sum of the two components is not presented here. This is also the case for the subharmonic $\langle v\rangle_{f/2}$ which becomes dominant at the end of the measuring domain for the TFW excitation and dominates the flow beyond $X > 600$ mm for the TFS case.

Most of the coherent energy for the SF excitation is contained in the fundamental frequency with the subharmonic being insignificant everywhere (figure 13). For the TFS excitation, the initial forcing levels at f_0 and at $\frac{1}{2}f_0$ were comparable, however,

while the fundamental hardly amplified the subharmonic soared. It is worth mentioning that the interactive mode, $\frac{3}{2}f_0$, may play an important role in both TFW and TFS experiments. Its integrated energy attained the same level as the fundamental around $X = 350$ mm in the TFS case while exceeding the energy content of the subharmonic around $X = 500$ mm (figure 13*b*) in the TFW experiment. In both the TFW and TFS cases, the subharmonic frequency was rapidly amplified after the fundamental started to decay, suggesting possible energy exchange between the fundamental and the subharmonic.

The contributions of the individual components to the Reynolds stress are shown in figure 13(*c*). At small values of X, most of the coherent Reynolds stress is contained in the fundamental excitation frequency for the SF and the TFW flows, but not in the TFS case that contains coherent stresses at f_0, $\frac{1}{2}f_0$ and many higher harmonics. These are associated with the high forcing amplitudes. Wherever $\int\langle uv\rangle_f \mathrm{d}y$ becomes negative during the SF experiment so does the integrated Reynolds stress $\int u'v'\mathrm{d}y$. The latter changes sign (to become positive again) around $X = 840$ mm owing to the contribution of random motion (figure 13*c*). In the TFW excitation the negative $\int\langle uv\rangle_f \mathrm{d}y$ is offset by the positive $\int\langle uv\rangle_{f/2}\mathrm{d}y$ making the overall Reynolds stress still negative, but over a very short region. The positive contribution of the subharmonic $\int\langle uv\rangle_{f/2}\mathrm{d}y$ in the TFS case overwhelms the negative Reynolds stress associated with the fundamental frequency, thus retaining a positive stress throughout the flow. In fact, the slope of $\int\langle uv\rangle_{f/2}\mathrm{d}y$ with X increased tremendously at the very same location at which $\int\langle uv\rangle_f \mathrm{d}y$ became negative (i.e. at $X = 350$ mm). At this very location, the overall turbulence production for the TFS flow had its minimum (figure 1). This suggests that the coherent motion associated with the fundamental frequency transfers energy to the subharmonic and it may do so because of resonance. The contribution of the $\frac{3}{2}f_0$ frequency to the Reynolds stress is negligible for all three types of excitation used, although its energy content is significant, particularly in the TFS case. This leads us to believe that the $\frac{3}{2}f_0$ mode does not interact with the mean motion but rather with the two forced waves.

3.6. *Vorticity balance*

Before discussing further the role of the coherent structures in this flow and their effects on the vorticity distribution, we should verify that the phase-locked and ensemble-averaged vorticity field derived from the measured velocity field is indeed correct. Thus, the vorticity balance was tested. Reynolds decomposition of the equations of motion into steady and random components renders the turbulent energy budget that expresses the interaction between the mean motion and the turbulence through the production term. Triple decomposition into mean, coherent and random motion (Hussain 1983) yields a coherent energy equation that explains the interaction between the coherent and the mean energy through the production term; it also provides for the interaction between the coherent and the random components of energy through the intermodal production term. However, this equation does not provide information about the interactions that occur among the coherent motions themselves, and this can be provided by the vorticity equation. Thus, a vorticity balance will enable us to explore the nonlinear wave interactions.

According to Hussain (1983), the rate of change of the mean vorticity is given by:

$$\frac{\bar{\mathrm{D}}}{\mathrm{D}t}\Omega_i = \underbrace{\Omega_j\frac{\partial U_i}{\partial x_j}}_{\mathrm{I}} + \underbrace{\nu\frac{\partial^2\Omega_i}{\partial x_k\partial x_k}}_{\mathrm{II}} + \underbrace{\frac{\partial}{\partial x_j}(\overline{u_{Ci}\omega_{Cj}} - \overline{u_{cj}\omega_{ci}})}_{\mathrm{III}} + \underbrace{\frac{\partial}{\partial x_j}(\overline{u_{ri}\omega_{rj}} - \overline{u_{rj}\omega_{ri}})}_{\mathrm{IV}},$$

where the first term on the right-hand side of the equation represents the stretching and twisting of the mean vorticity by the mean velocity gradients. The second term represents the viscous diffusion to the mean vorticity. The third term represents the time-averaged interaction (i.e. stretching and convection) between the coherent vorticity and the coherent velocity fluctuations, while the fourth term does the same for the random motion.

Similarly, the substantial derivative of the coherent vorticity:

$$\frac{\mathrm{D}\omega_{Ci}}{\mathrm{D}t} = \underset{\text{I}}{\omega_{Cj}\frac{\partial U_i}{\partial x_j}} + \underset{\text{II}}{\Omega_j\frac{\partial u_{Ci}}{\partial x_j}} + \underset{\text{III}}{\nu\frac{\partial^2\omega_{Ci}}{\partial x_k\partial x_k}} + \underset{\text{IV}}{\frac{\partial}{\partial x_j}(u_{Ci}\omega_{Cj} - \overline{u_{Ci}\omega_{Cj}})}$$

$$- \underset{\text{V}}{\frac{\partial}{\partial x_j}(\omega_{Ci}u_{Cj} - \overline{\omega_{Ci}u_{Cj}})} - \underset{\text{VI}}{\frac{\partial}{\partial x_j}(u_{Cj}\Omega_i)} + \underset{\text{VII}}{\frac{\partial}{\partial x_j}(\langle u_{ri}\omega_{rj}\rangle - \overline{u_{ri}\omega_{rj}})}$$

$$- \underset{\text{VIII}}{\frac{\partial}{\partial x_j}(\langle\omega_{ri}u_{rj}\rangle - \overline{\omega_{ri}u_{rj}})}$$

is balanced by the sum of the eight terms on the right-hand side of the equation. Now, however, the first term on the right-hand side represents the stretching of the coherent vorticity by the mean velocity gradients while the second term represents the stretching of the mean vorticity by the coherent velocity gradients. The third term yields the viscous diffusion of the coherent vorticity. The fourth and fifth terms represent the residual coherent (after subtracting the mean) interaction between the coherent vorticity and the coherent velocity fluctuations. They again represent the stretching and convection of the coherent vorticity that is analogous to the third term in the mean vorticity equation. The sixth term represents the convection of mean vorticity by the coherent eddies, while the seventh and eighth terms the residual coherent (after subtracting the mean) interaction between the random vorticity and random velocity fluctuations.

By assuming that the coherent motion is principally two-dimensional, the streamwise component of the coherent vortices may be neglected. We may also assume that the influence of the random motion is secondary and negligible and therefore terms I, IV and the first portion of term III can be dropped from the mean vorticity equation. For the same reason, terms I, II, IV, VII and VIII on the right-hand side of the coherent vorticity equation can also be neglected.

The rate of change of mean vorticity (left-hand side of the mean vorticity equation) was calculated directly from the measured mean velocities for typical x-locations and plotted using discrete symbols in figure 14. The lines represent the same quantity that was calculated from the right-hand side of the equation and required phase-locked and ensemble-averaged input. The good agreement between the two sets of data indicates that the measurements and the assumption of two-dimensionality of the coherent structures are valid. The calculations suggested that the viscous diffusion term can also be neglected, thus, the rate of change of the mean vorticity is only caused by the time-averaged convection of the coherent vorticity by the coherent velocity. In other words, the changing distribution of the mean vorticity across the flow and consequently the spreading rate of the entire mean velocity field is caused by the nonlinear interaction between coherent motions.

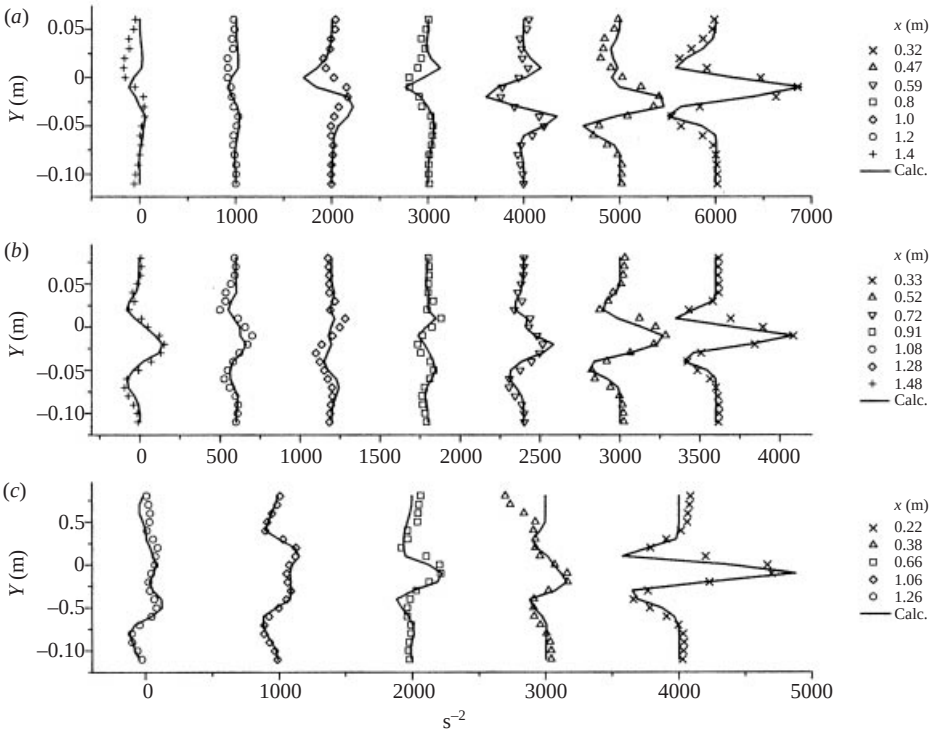

FIGURE 14. Mean vorticity balance. Symbols, measured rate of change of the mean vorticity (left-hand side of the equation; lines, calculated rate of change from the right-hand side of the equation. (*a*) SF. (*b*) TSW. (*c*) TFS.

The calculations based on the coherent vorticity equation were not as satisfactory, particularly near the borders of the mixing layer with the respective uniform streams and near the centre of the mixing layer. Thus, the results plotted in figure 15 are for two selected Y-locations on each side of the mixing layer only; they contain, however, all three data sets: SF, TFW, TFS. The agreement between the calculations and the measurements (i.e. representing both sides of the coherent vorticity equation) is qualitatively reasonable. The discrepancies attributed to the lack of two-dimensionality and to the terms representing the random motion (terms VII and VIII) that probably should not have been neglected. Since the viscous diffusion term was again negligible, the rate of change of the coherent vorticity is balanced by terms V and VI in the equation (i.e. the convection of coherent and mean vorticity by the coherent eddies).

3.7. *Coherent vorticity*

The isodynes (vorticity contours) plotted in figure 16 were calculated from the two-dimensional, phase-locked and simply ensemble-averaged data at two phases separated by a single period of the fundamental excitation, $\Phi_{fun} = 2\pi$. They show the interactions between adjacent, coherent vortices and they provide a visual basis for comparing the three experiments, SF, TFW, TFS. The time-averaged results of these interactions are rooted in the vorticity balance described above. Only the most relevant isodynes are shown in figure 16 because some of this data was published elsewhere together with the associated streaklines (Wygnanski & Weisbrot 1988). The label Φ_{fun} in figure 16 is an arbitrarily chosen reference phase to guide the reader to

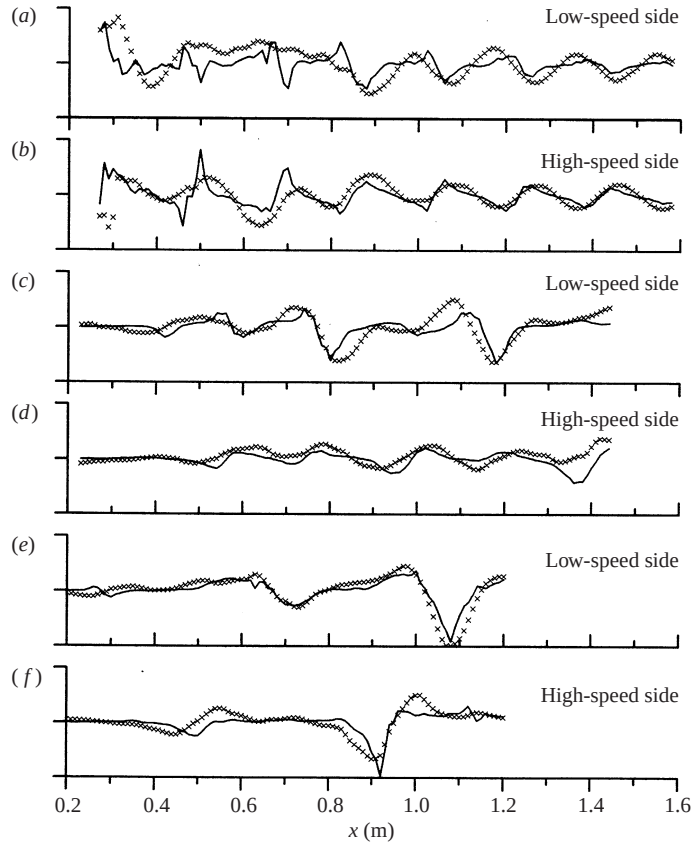

FIGURE 15. Coherent vorticity balance. Symbols, measured rate of change of the coherent vorticity (left-hand side of the equation); lines, calculated rate of change from the right-hand side of the equation. (*a*), (*b*) SF. (*c*), (*d*) TFW. (*e*), (*f*) TFS.

the difference in the two patterns with a time interval of one fundamental period. An attempt was made to sharpen those images by using the temporal pattern recognition technique (Zhou *et al.* 1996), but the improvement in the results did not warrant the added complexity.

The coherent structures in the SF case (for $X > 500$ mm, corresponding to the location where the linear amplification of the disturbances at the fundamental frequency ceases) are well represented by a single row of vortices, whose strength diminishes with increasing X. These vortices are equally spaced in the direction of streaming and are aligned with the mean centre of the flow (i.e. $Y_{0.5}$). For the TFW case, adjacent vortices are staggered slightly around the mean centreline owing to the imposed subharmonic perturbation. This leads to a mutual induction that results in a decrease of the streamwise distance between them as they proceed downstream (compare figure 16, numbers 4 and 5), leading to possible pairing beyond the measurement domain. The lateral displacement of adjacent pairs of vortices in the TFS case is much larger, even at small values of X, and that enables their amalgamation within the measurement domain (figure 16*c*, numbers 5 and 6). The large, lateral displacement of these eddies causes the observed distortions in the mean velocity (figure 3), and results in the peculiar distribution of amplitudes of the leading frequencies contained in these coherent structures (see figure 12). Since the levels contained in the coherent

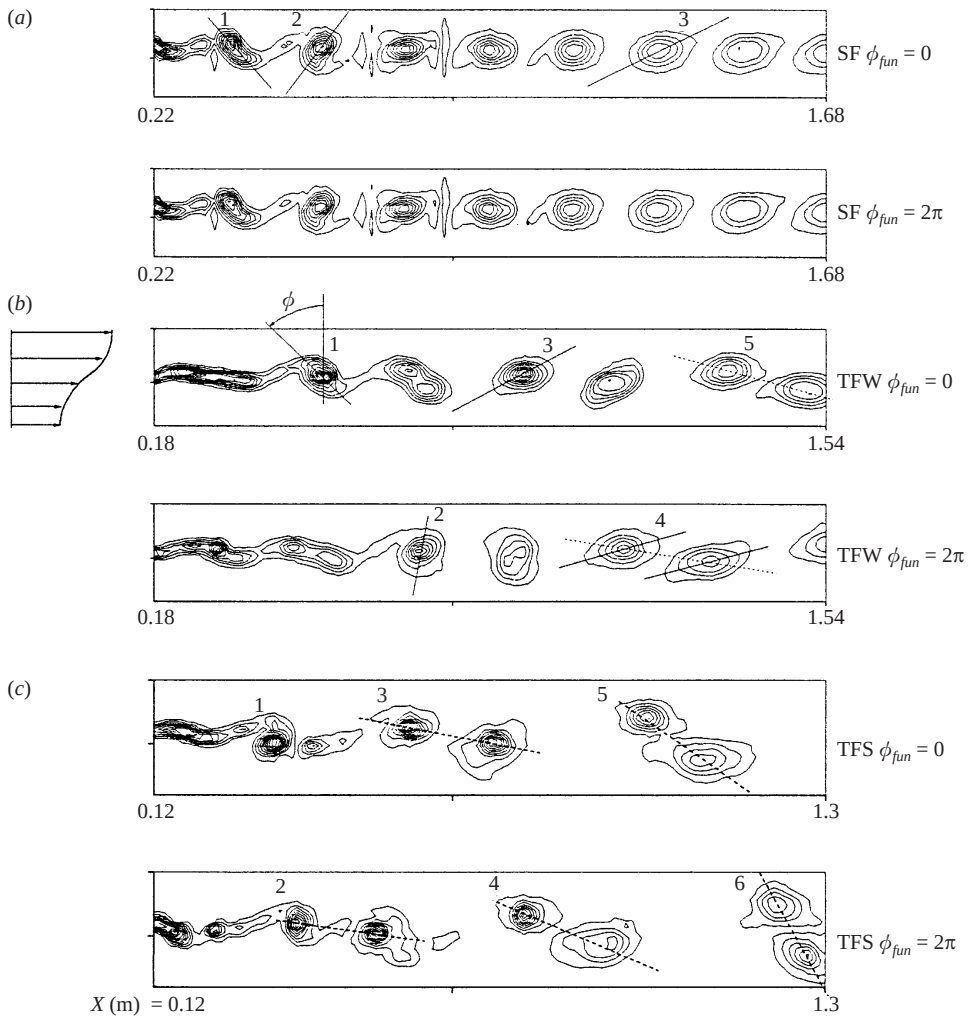

FIGURE 16. Vorticity contours of the forced mixing layer. ——, fundamental; – – –, subharmonic.

parts of the motion dominate the flow, they may even be observed in the turbulent intensity distribution shown in figure 5(*c*).

The vortices displaced toward the high-velocity side (upward in figure 16) in the TFW case retain their strength much further downstream than the vortices displaced downward (i.e. toward the low-velocity side). However, the relative strength of adjacent vortices in the TFS case oscillates with increasing streamwise distance. This suggests that there is a periodic exchange of vorticity and presumably energy between such pair of vortices during their amalgamation process. Initially, the strength of the vortex that is displaced upward increases with X while the vorticity contained in the one displaced downward (toward the lower-velocity side in figure 16*c*) is quickly depleted (compare numbers 2, 3 and 4 in figure 16*c*). The process is reversed for $X > 1200$ mm (see numbers 5 and 6 in figure 16*c*).

The Reynolds stress distribution is also closely related to the shape and inclination of the isodynes, as was suggested by Browand & Ho (1983) and by Hussain (1983). When an eddy represented by a closed vorticity contour is tilted backward (i.e. it is

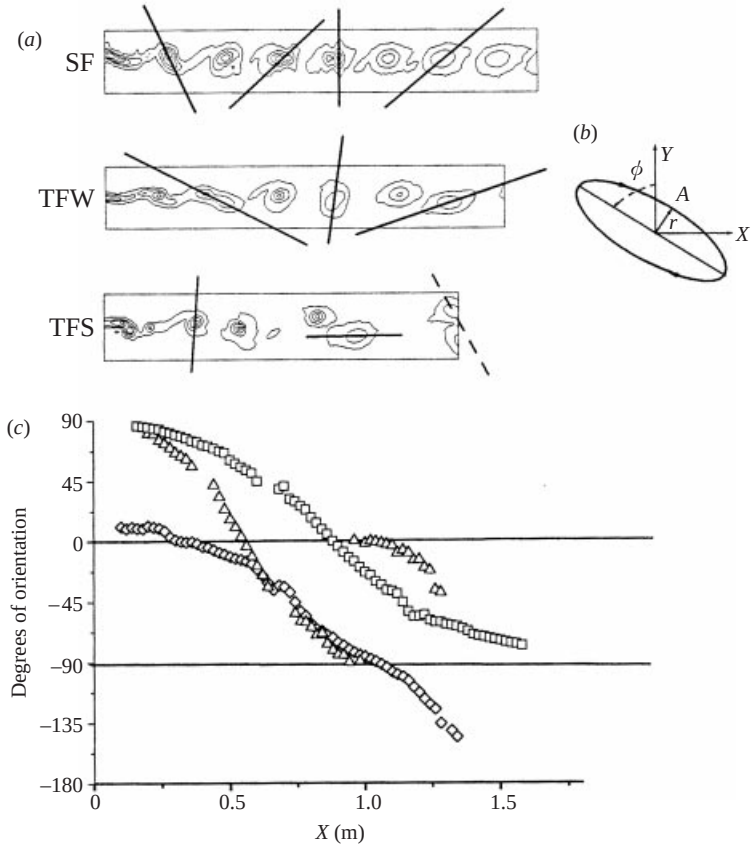

FIGURE 17. Calculated orientation of spanwise coherent vortices. △, SF; □, TFW; ◇ TFS.

advanced more on the low-velocity side than on the high-velocity side), the Reynolds stress that it generates is positive. When it is tilted forward, its contribution to the Reynolds stress is negative. Amplified, wavy perturbations are associated with vortices that are tilted backward whereas decaying ones are always tilted in the forward direction (Michalke 1964; Wygnanski & Weisbrot 1988). We may also filter the phase-locked and ensemble-averaged signals and determine the frequency that dominates the isodynes and whether that mode decays or amplifies. For example: eddy number 1 in the SF case (figure 16*a*) amplified while 2 starts to decay and the decay rate of 3 is even larger. In the TFW flow, eddy number 1 is amplified, 2 is almost neutral, while the fundamental modes 3 and 4 (shown as single vorticity concentrations in figure 16*b*) that are further downstream, decay. The combination of the two vortices (figure 16*b* number 5) indicates amplification at the subharmonic frequency since the line connecting the two centres is tilted backward. A similar observation can also be made for the TFS experiment where the rate of amplification of the subharmonic mode increases up to the maximum at vortex pair 5 (angle of inclination approximately 45°) and then decreases at large X (6 in figure 16*c*).

The relation between the inclination of a coherent vortex to the flow direction (marked by the angle ϕ in figures 16*b* and 17*b*) and the coherent Reynolds stress that it generates may be quantified by assuming that such an eddy conserves its angular momentum. Consequently, $(u'^2 + v'^2)r = C$, where u' and v' are the coherent velocity

components and r is the distance of the typical point on the control surface from the centre of the vortex (figure 17*b*). C is a constant defining the intensity of the circulation in the vortex.

Assuming that only the orientation of the vortex varies during its movement downstream, the coherent velocity induced by such a vortex will not change for an observer moving with the vortex. Thus, the relation between the $u'v'$ and the vortex orientation can be found by considering any point that is fixed relative to the vortex. For simplicity, a point located at the end of the minor axis (see point A marked on figure 17*b*) is chosen for this purpose. Thus,

$$u' = \sqrt{\frac{C}{r}}\sin\phi, \quad -v' = \sqrt{\frac{C}{r}}\cos\phi, \quad -u'v' = \frac{C}{2r}\sin(2\phi).$$

Consequently,

$$\int_{-\infty}^{\infty}\int_{-\infty}^{\infty}(-u'v')\,\mathrm{d}x\,\mathrm{d}y = \tfrac{1}{2}C\sin(2\phi)\int_{-\infty}^{\infty}\int_{-\infty}^{\infty}\frac{1}{r}\mathrm{d}x\,\mathrm{d}y. \tag{1}$$

For a particular vortex, the maximum or minimum integral of the coherent Reynolds stress should occur wherever $\sin(2\phi) = \pm 1$ or the inclination of the vortex is $\phi = \pm 45°$. Thus,

$$\left[\int_{-\infty}^{\infty}\int_{-\infty}^{\infty}(-u'v')\,\mathrm{d}x\,\mathrm{d}y\right]_{\max} = \tfrac{1}{2}C\int_{-\infty}^{\infty}\int_{-\infty}^{\infty}\frac{1}{r}\mathrm{d}x\,\mathrm{d}y. \tag{2}$$

Dividing equation (1) by (2) gives,

$$\phi = \tfrac{1}{2}\arcsin\left[\frac{\displaystyle\int_{-\infty}^{\infty}\int_{-\infty}^{\infty}(-u'v')\,\mathrm{d}x\,\mathrm{d}y}{\left(\displaystyle\int_{-\infty}^{\infty}\int_{-\infty}^{\infty}(-u'v')\,\mathrm{d}x\,\mathrm{d}y\right)_{\max}}\right]$$

The integration along X can be replaced by the integration over time that yields:

$$\phi = \tfrac{1}{2}\arcsin\left[\frac{\displaystyle\int_{-\infty}^{\infty}(-\overline{u'v'})\mathrm{d}y}{\left(\displaystyle\int_{-\infty}^{\infty}(-\overline{u'v'})\mathrm{d}y\right)_{\max}}\right].$$

The calculated inclination angles of the fundamental coherent vortices based on the Reynolds stress (figure 13) are shown in figure 17(*c*) and are compared to the vorticity contours in figure 17(*a*). For the SF case, the fundamental component of the Reynolds stress is maximum at $X = 300$ mm while vanishing at $X = 550$ mm before attaining a minimum negative stress at $X = 700$ mm. The corresponding calculated inclination angles of the isodynes (figure 17*a*) corroborate these findings $\phi = +45°$ at $X = 300$ mm, $\phi = 0°$ at $X = 550$ mm at $\phi = -45°$ at $X = 700$ mm. We may also compare the calculated values with isodynes (considering the fundamental only) in the TFW and TFS cases. The good agreement between the two very different sets of measurements, suggest that the correlation between them is high.

If, however, we are concerned with the coherent Reynolds stress of the subharmonic, we may consider adjacent pairs of vortices as shown in figures 16*b* and 16*c* (numbers 4 and 5) or filter the coherent vorticity so that it includes the subharmonic only. In the TFS case, the maximum coherent Reynolds stress at the subharmonic frequency

occurred at $X = 1100\,\text{mm}$ and it corresponds to $\phi_{f_0/2} = +45^\circ$ (see figure 16*c* number 5).

3.8. *The conditions for resonance and the definition of a dominant mode*

In many instances (for the SF excitation in particular), the energy contained within the coherent structures increases or decreases depending on the sign of the coherent Reynolds stress (figure 13*c*). It implies that the coherent eddies exchange energy with the mean motion, mostly extracting energy from it, via the production term $\langle uv \rangle \mathrm{d}U/\mathrm{d}Y$. This, however, is not always the case, as was observed for the TFS excitation (figure 13*c*). Here, the energy contained in the fundamental mode increases in the direction of streaming (for $X > 380\,\text{mm}$) despite the fact that the shear stress associated with this mode is negative between $X = 380\,\text{mm}$ and $1060\,\text{mm}$. On the other hand, the energy contained in the fundamental mode follows the positive production term and increases beyond $X = 1060\,\text{mm}$. The mismatch between the increase in the energy contained by a specific mode and the production term for this mode implies that the energy comes from sources other than the mean motion and a resonance is suspected. Again, the oscillatory interchange of the intensity of circulation between adjacent pairs of vortices or between the two vortices within a pair in the TFS flow (figure 16*c*) also suggest that a resonant interaction might have taken place between the fundamental and the subharmonic.

The standard conditions for triad resonance in parallel shear flow that is concomitantly excited by two wavy disturbances, f_0 and $\frac{1}{2}f_0$ are:

$$\alpha_{res} = \alpha_{f_0} \pm \alpha_{f_0/2}$$

$$\beta_{res} = \beta_{f_0} \pm \beta_{f_0/2}$$

where β is the frequency and α is the wavenumber. Whenever the instabilities are evolving in space, α is complex ($\alpha = \alpha_r + \mathrm{i}\alpha_i$) while β is real and determined by the excitation frequency. In the present experiment β_{res} might be associated with the subharmonic, $\frac{1}{2}f_0$ (that is also the difference between the imposed frequencies), or with their sum $\frac{3}{2}f_0$. In order that the two primary waves will exchange energy between them, they have to travel together, i.e. their phase velocity, $c_{ph} = \beta/\alpha_r$, has to be identical over some region. In parallel flows, excited at constant frequencies, this may be a frequent occurrence because α is constant across the flow (i.e. $\alpha = \alpha(x)$ only), but in a divergent mean flow of the kind considered presently, the regions of possible interaction are more limited since $\alpha = \alpha(x, y)$. Another complicating factor is that energy can be exchanged between the coherent eddies and the mean flow that in turn responds by changing its rate of divergence in the direction of streaming and/or by becoming distorted.

The phase velocities of the dominant disturbances were calculated for the entire flow field and for the three experiments considered. A sample of those c_{ph} representing the variation of the $\langle v \rangle$ component with x are plotted in figure 18 for three locations across the flow: on the high-velocity side ($Y \approx 100\,\text{mm}$), in the centre ($Y \approx 0$) and on the low-velocity side ($Y \approx -110\,\text{mm}$). The $\langle v \rangle$ component was selected because it is the most amplified component of the flow, its amplitude is large in the central region of the mixing layer and it does not reverse its phase in the centre. The phase velocity of the fundamental mode that is the only frequency of significance in the SF experiment, is approximately constant everywhere and roughly equal to $U_c = 0.5(U_1 + U_2)$. The phase velocity of the fundamental mode in the TFW case is also constant throughout the flow, but the other two modes oscillate around it. These oscillations diminish with

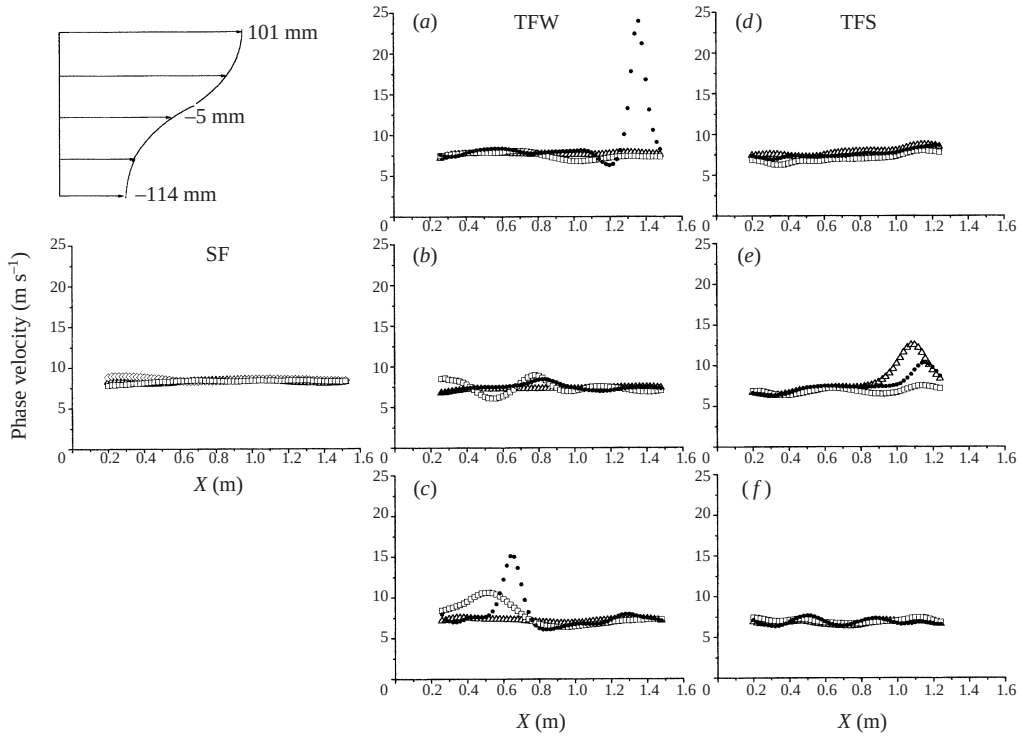

FIGURE 18. Streamwise phase velocity distribution of the coherent waves. For SF: △, $y = -114$ mm; ◇, −5 mm; □, 80 mm. For TFW and TFS: △, fundamental; □, subharmonic; ●, $\frac{3}{2}f_0$. (*a*), (*d*) $Y = 101$ mm; (*b*), (*e*) −5 mm; (*c*), (*f*) −114 mm.

x in the central region of the flow (i.e. at $Y = -5$ mm) and they are hardly significant beyond $x > 1000$ mm (see figure 18*b*). On the high-speed side of the flow, all three modes travel together up to $x = 1200$ mm whereupon the $\frac{3}{2}f_0$ mode undergoes a rapid acceleration (figure 18*a*). On the low-velocity side of the flow, the three waves locked in phase at $x > 800$ mm. For $800 < x < 1200$, there is a reasonable lock-in among all three waves across the entire width of the flow. In this region, however, the mean flow is slightly contracting (figure 1) owing to the negative production associated with the decaying fundamental mode (figure 13*c*).

The ordinate in figure 19 represents the rate of amplification of a given mode defined by $\theta d/\mathrm{d}x\{\log[\int(\langle v\rangle^2 + \langle u\rangle^2)_f \mathrm{d}Y]/[\int(\langle v\rangle^2 + \langle u\rangle^2)_f \mathrm{d}Y]_0\}$. When a single wave develops in a linear manner owing to the instability of the mean motion, this quantity is analogous to-$\alpha_i\theta/R$. The fundamental mode amplifies and decays in a manner consistent with a linear model. During its decay (for $x > 800$ mm), it probably transfers some energy to the mean motion because the production term of the fundamental is negative and the mean flow responds by reversing its lateral rate of spread (figure 1). A reduction in the energy thickness (that behaves like θ) indicates a gain in the mean energy.

In TFW, the energy contained in the subharmonic mode keeps increasing (figure 13) and its rate of increase does not diminish between 800 and 1200 mm from the origin (figure 19). A linear model would have predicted a reduction in that rate which would presumably be parallel to the reduction in the fundamental, f_0. The $\frac{3}{2}f_0$ component lost energy in this x interval (figure 13), as it also appears in

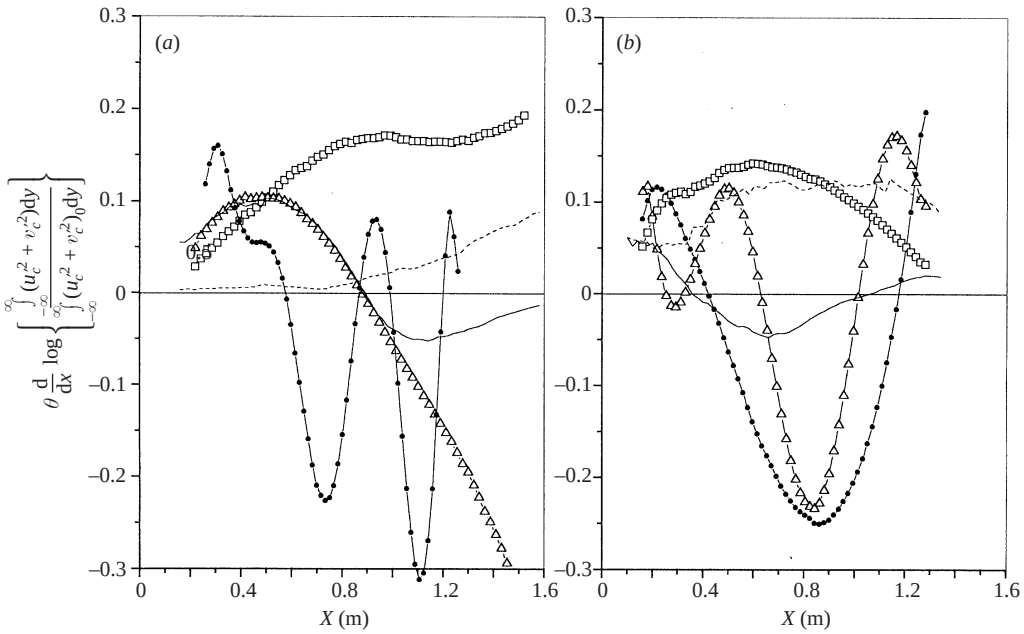

FIGURE 19. The amplification rate of coherent energy. (*a*) TFW. (*b*) TFS. △, f_0; □, $\frac{1}{2}f_0$; ●, $\frac{3}{2}f_0$; ——, $\frac{1}{5}$prod f_0; – – –, $\frac{1}{5}$prod $\frac{1}{2}f_0$(m^3 s^{-3}).

figure 19. Thus, in this range of streamwise locations, the amplification and decay of f_0 and $\frac{1}{2}f_0$ is enabled by a transport of energy from the mean flow (through the production of the fundamental) and by decay of the $\frac{3}{2}f_0$ mode. The incoherent motion also decreases in intensity in this region (i.e. for $800 < x < 1200$ mm) eliminating the possibility of energy transfer to the random, smaller-scale eddies. Thus, the dominant mode, over most of the measurement domain (for $x < 1300$ mm, see figure 13*b*), is the fundamental mode that behaves in a manner reminiscent of the linear development.

Under ideal (linear) development, the subharmonic mode should have attained its largest rate of amplification where the fundamental becomes neutrally stable (i.e. around $x = 850$ mm; figure 19*a*). It could have then amplified further (Kelly 1967) if it were to receive energy from the fundamental. This is probably not the case in this flow, since the rate of amplification of the subharmonic remained constant in this region (i.e. for $850 < x < 1300$) and the total mean energy also did not change (the rate of spread of the mixing layer stopped). The resonance proposed by Kelly might have occurred at larger distance (i.e. at $x > 1300$ mm) where the rate of decay of the fundamental and the rate of amplification of the subharmonic have both increased. The two modes travelled together (figure 18*a–c*) and during this interval the amplitude of the subharmonic increased greatly (figure 13). The most plausible explanation for this exchange of energy is resonance.

In contrast to the TFW experiment, the phase velocity of the subharmonic in the TFS cse keeps almost constant throughout the entire measurement domain. The phase velocities of f_0 and $\frac{3}{2}f_0$ are almost identical to the subharmonic on both sides of the flow, but differ from it in the central region for $x > 850$ mm (figure 18*c*). Around this streamwise location, the decay rates of both of these modes attained their maximum. The fundamental mode starts to amplify for $x > 1000$ mm, at this x

its phase velocity is sufficiently different from the subharmonic's and it can no longer transfer energy to it. The $\frac{3}{2}f_0$ mode follows suit around $x = 1200$ mm and resumes its amplification while the amplification rate of the subharmonic decreases in this region (figure 19). Consequently, the subharmonic appears to be the dominant wave in the TFS experiment.

Yao (1999) suggested that the mean flow is involved in the resonance and it can be considered as a wave of zero frequency and an infinite wavelength. It contributes to the energy transfer between the fundamental and the subharmonic and sometimes has the role of a catalyst in the process. Therefore, the production term of an individual mode (e.g. $\langle uv\rangle_{f_0}\mathrm{d}U/\mathrm{d}y$) does not conflict with the concept of resonance. Consequently, the integrated production rates of f_0 and of $\frac{1}{2}f_0$ across the flow are plotted on figure 19. The spectra presented in figure 8 indicate that f_0 is the dominant mode in the TFW experiment. This dominance is shared among all three major waves ($\frac{1}{2}f_0$, f_0, and $\frac{3}{2}f_0$) near the origin of the TFS experiment, but it ends with the dominance of $\frac{1}{2}f_0$ in the last 50% of the measurement domain.

4. Concluding remarks

The turbulent mixing layer is very sensitive to external, two-dimensional excitation because the momentum transport across it is mostly coherent. In some instances, more than 90% of the ensuing Reynolds stress is even contained within the excitation frequency. Furthermore, by exciting the flow at two frequencies, a fundamental and a subharmonic, the resulting Reynolds stresses remain large and coherent throughout the test section. This is not the case when the flow is excited at a single frequency. Calculations based on the two-dimensional mean momentum and vorticity equations suggest that the mean flow and the large coherent eddies are predominantly two-dimensional. Reasonable mean and coherent vorticity balances were attained by assuming both components to be two-dimensional and totally neglecting the influence of random motion. This opened the possibility of correlating the coherent Reynolds stresses to the deformation and orientation of the spanwise coherent vortices.

The dramatic increase in Reynolds stress resulting from simultaneous excitation at the fundamental and subharmonic frequencies is associated with a resonance phenomenon that extracts energy from the mean motion or from the fundamental excitation frequency depending to a large extent on the level of the excitation. When the level of the subharmonic frequency is high, it quickly dominates the flow and the measure of this dominance may be assessed by the linear-like behaviour of this mode. This might be tested by its relation to the rate of spread of the mean flow. For a mean velocity profile that can be approximated by a hyperbolic tangent {i.e. $U = \frac{1}{2}[1 + \tanh(y)]$}, a linear perturbation attains its maximum amplitude (i.e. becomes neutrally stable) where $f\theta/U_c = 0.08$. This number was reached at $x = 850$ mm for the TFW case where the dominant frequency considered in the above equation was f_0. The same number was attained near the end of the measurement domain (around $x = 1350$ mm) for the TFS case, but the dominant frequency considered in this case was $\frac{1}{2}f_0$. Therefore, the quantity $f\theta/U_c = 0.08$ may serve as a first-order criterion for the determination of the dominant mode in a flow excited by a multitude of periodic perturbations. All the results collapse approximately onto a single curve (figure 20*b*) when the measured $f\theta/U_c$ is scaled with RfX/U_c where f is the dominant frequency, U_c is the measured phase velocity at the dominant frequency and $R = (U_1 - U_2)/(U_1 + U_2)$. This was done for the single-frequency excitation by

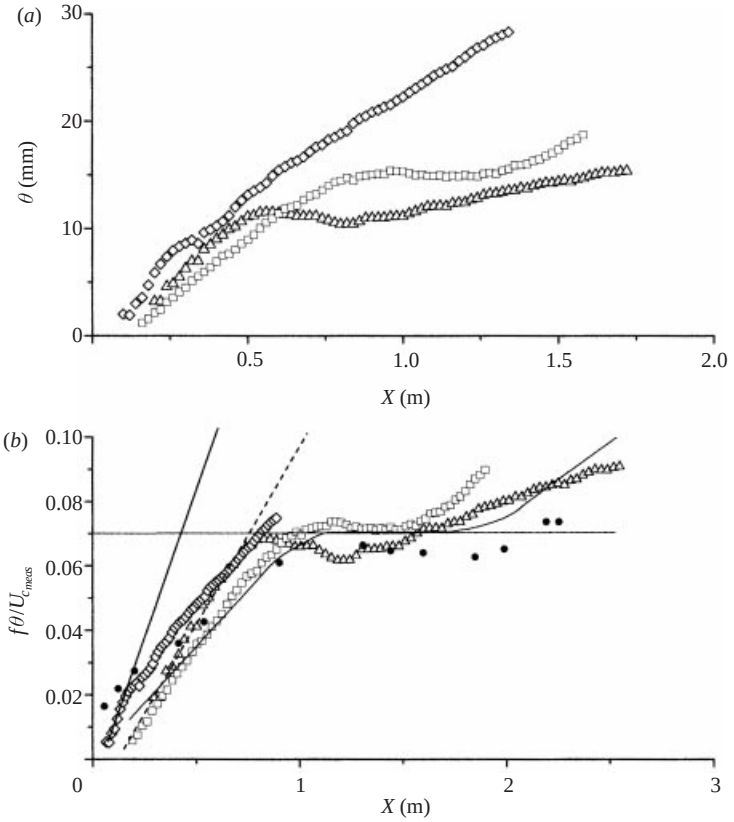

FIGURE 20. Streamwise distribution of the momentum thickness (*a*) in physical dimensions, (*b*) normalized by dominant frequency and measured phase velocity. △, SF; □, TFW; ◇, TFS; ——, Wygnanski & Petersen (1987); ●, Browand & Ho (1983).

Browand & Ho (1983) whose data (quoting Ho & Huang 1982) is also reproduced in the figure.

The practical advantage of exciting the flow at two frequencies simultaneously becomes self evident when we assume that the dimensionless saturation thickness based on the predominant frequency remains unchanged. The excitation at the fundamental frequency is advantageous at small X because the mean flow amplifies this frequency more rapidly than its subharmonic and it responds by spreading faster initially (figure 20*a*). However, if the subharmonic has a substantial amplitude at the saturation location of the fundamental, it may extract energy from it through resonance and thus dominate the rate of spread of the mixing layer as long as it did not reach its new dimensionless saturation value (figure 20*b*). This technique enables the mixing layer to become twice as wide at a prescribed distance from its origin. Since the large coherent eddies control the scalar transport and the rate of chemical reaction (Roberts 1985) the concomitant excitation of the flow at both frequencies has its payoffs. It should also have an impact on the effectiveness of the control of separation by periodic excitation because it depends on the rate of entrainment of ambient fluid by the mixing layer near a solid surface.

This research was supported by AFOSR grant number F49620-96-1-0187 monitored by Drs J. McMichael and T. Beutner. The authors also wish to thank Mr I. Weisbrot

(formerly at Tel Aviv University) who measured the three sets of mixing-layer data, which were adopted as the database of this paper.

REFERENCES

Acton, E 1976 The modelling of large eddies in a two-dimensional shear layer. *J. Fluid Mech.* **76**, 561.

Ashurst, W. T. 1979 Numerical simulation of turbulent mixing layers via vortex dynamics. In *Turbulent Shear Flows*, vol. 1, p. 402.

Browand, F. K. 1966 An experimental investigation of the instability of an incompressible, separated shear layer. *J. Fluid Mech.* **21**, 281.

Browand, F. K. & Ho, C. M. 1983 The mixing layer: an example of quasi two-dimensional turbulence. *J. Méc. Theor. Appl.* Special volume, 99.

Browand, F. K. & Weidman, P. D. 1976 Large scales in the developing mixing layer. *J. Fluid Mech.* **76**, 127.

Brown, G. L. & Roshko, A. 1974 On density effects and large structure in turbulent mixing layers. *J. Fluid Mech.* **64**, 775.

Corcos, G. M. & Sherman, F. S. 1984 The mixing layer: deterministic models of a turbulent flow. Part 1. Introduction and the two-dimensional flow. *J. Fluid Mech.* **139**, 29.

Crighton, D. G. & Gaster, M. 1976 Stability of slowly diverging jet flow. *J. Fluid Mech.* **77**, 397.

Fiedler, H. E., Dziomba, B., Mensing, P. & Rosgen, T. 1981 Initiation, evolution and global consequences of coherent structures in turbulent shear flows. Lecture Notes in Physics, vol. 136, p. 219. Springer.

Fiedler, H. E. & Mensing, P. 1985 The plane turbulent shear layer with periodic excitation. *J. Fluid Mech.* **150**, 281.

Freymuth, P. 1966 On transition in a separated laminar boundary layer. *J. Fluid Mech.* **25**, 683.

Gaster, M., Kit, E. & Wygnanski, I. 1985 Large scale structures in a forced turbulent mixing layer. *J. Fluid Mech.* **150**, 23.

Ho, C. M. & Huang, L. S. 1982 Subharmonics and vortex merging in mixing layers. *J. Fluid Mech.* **119**, 443.

Hussain, A. K. M. F. 1983 Coherent structures – reality and myth. *Phys. Fluids* **26**, 2816.

Inoue, O. & Leonard, A. 1987 Vortex simulation of forced/unforced mixing layers. *AIAA Paper* 87-0288.

Inoue, O. 1989 Artificial control of turbulent mixing layers. *Proc. Second IUTAM Symposium on Structure of Turbulence and Drag Reduction. Zurich, Switzerland, 25–28 July 1989.*

Inoue, O. 1992 Double-frequency forcing on spatially growing mixing layer. *J. Fluid Mech.* **234**, 553.

Katz, Y., Nishri, B. & Wygnanski, I. 1989 The delay of turbulent boundary-layer separation by oscillatory active control. *AIAA paper* 89-0975; also *Phys. Fluids* A **1**, 179.

Kelly, R. E. 1967 On the stability of an inviscid shear layer which is periodic in space and time. *J. Fluid Mech.* **27**, 657.

Michalke, A. 1964 On the inviscid instability of the hyperbolic tangent velocity profile. *J. Fluid Mech.* **19**, 543.

Monkewitz, P. A. & Huerre, P. 1982 The influence of velocity ratio on the spatial instability of mixing layers. *Phys. Fluids* **25**, 1137.

Neuburger, D. & Wygnanski, I. 1988 The use of a vibrating ribbon to delay separation on two-dimensional airfoils. *Proc. Air Force Academy Workshop on Separated Flow*, F. J. Seiler Research Labs. Rep. TR-88-0004.

Oster, D. & Wygnanski, I. 1982 The forced mixing layer between parallel streams. *J. Fluid Mech.* **123**, 91.

Oster, D., Wygnanski, I., Dziomba, B. & Fiedler, H. 1978 The effects of initial conditions on the two-dimensional mixing layer. In *Structure and Mechanisms of Turbulence* (ed. H. Fiedler). Lecture Notes in Physics, vol. 75, p. 48. Springer.

Paschereit, C. O., Wygnanski, I. & Fiedler, H. E. 1995 Experimental investigation of subharmonic resonance in an axisymmetric jet. *J. Fluid Mech.* **283**, 365.

Patnaik, P. C., Sherman, F. S. & Corcos, G. M. 1976 A numerical simulation of Kelvin–Helmholtz waves of finite amplitude. *J. Fluid Mech.* **73**, 215.

Riley, J. J. & Metcalfe, R. W. 1980 Direct numerical simulation of a perturbed turbulent mixing layer. *AIAA paper* 80-0274.

Roberts, F. A. 1985 Effects of a periodic disturbance on structure and mixing in turbulent shear layers and wakes. PhD thesis California Institute of Technology, Pasadena, CA.

Sato, H. 1960 The stability and transition of a two-dimensional jet. *J. Fluid Mech.* **7**, 53.

Weisbrot, I. & Wygnanski, I. 1988 On coherent structures in a highly excited mixing layer. *J. Fluid Mech.* **195**, 137.

Winant, C. D. & Browand, F. K. 1974 Vortex pairing, the mechanism of turbulent mixing layer growth at moderate Reynolds number. *J. Fluid Mech.* **63**, 237.

Wygnanski, I. & Fiedler, H. E. 1970 The two-dimensional mixing region. *J. Fluid Mech.* **41**, 327.

Wygnanski, I., Fiedler, H., Oster, D. & Dziomba, B. 1979 On the perseverance of a quasi-two-dimensional eddy structure in a turbulent mixing layer. *J. Fluid Mech.* **93**, 325.

Wygnanski, I. & Petersen, R. A. 1987 Coherent motion in excited free shear flows. *AIAA J.* **25**, 201.

Wygnanski, I. & Weisbrot, I. 1988 On the pairing process in an excited plane turbulent mixing layer. *J. Fluid Mech.* **195**, 161.

Yao, L. S. 1999 A resonant wave theory. *J. Fluid Mech.* **395**, 273.

Zhang, Y. Q., Ho, C. M. & Monkewitz, P. 1984 The mixing layer forced by fundamental and subharmonic. *Proc. IUTAM Symposium on Laminar–Turbulent Transition, Novosibirsk, USSR, 9–13 July 1984.*

Zhou, M. D., Heine, C. & Wygnanski, I. 1996 The effects of excitation on the coherent and random motion in a plane wall jet. *J. Fluid Mech.* **310**, 1.